Microstructures and rheology of hydrous synthetic magmatic suspensions deformed in torsion at high pressure.

Laurent Arbaret, Misha Bystricky, Rémi Champallier

Microstructures and rheology of hydrous synthetic magmatic suspensions deformed in torsion at high pressure

Laurent Arbaret : Institut des Sciences de la Terre d'Orléans, UMR 6113, Université d'Orléans, Centre National de la Recherche Scientifique, Orleans, France

Misha Bystricky : Geologisches Institut, ETH Zürich, Zurich, Switzerland

Now at Laboratoire des Mécanismes et Transferts en Géologie, Observatoire Midi-Pyrénées, Université de Toulouse,
Toulouse, France

Rémi Champallier : Institut des Sciences de la Terre d'Orléans, UMR 6113, Université d'Orléans, Centre National de la Recherche Scientifique,
Orleans, France

Abstract

The relationship between magma rheology and characteristic magmatic microstructures was investigated by performing high-temperature high-pressure deformation experiments on hydrous synthetic magmatic suspensions in the range of 0% to 76% solid fraction (alumina grains). Torsion experiments were conducted at 300 MPa confining pressure, temperatures ranging from 475°C to 1000°C and shear strain rates ranging from 2.0×10^{-5} to 2.1×10^{-3} s^{-1} up to total strains of 21.3. Flow is Newtonian for a solid fraction of $\varphi_s = 0.0–0.16$ with a log dynamic viscosity $\eta = 10.3$ Pa s (T = 500°C). A deviation from Newtonian behavior is observed for $\varphi_s > 0.16$ with an increase in apparent viscosity of about 1 order of magnitude between $\varphi_s = 0.16$ and 0.54. The shape fabric of the solid phase is characterized by a unimodal orientation that is almost stable and nearly parallel to the shear direction. Both shape fabric and deviation from Newtonian behavior originate from the increase in the number of particle clusters in the suspension. The apparent viscosity increases by 1.5 orders of magnitude between $\varphi_s = 0.54$ and 0.65, and extrapolation of the data suggests a very sharp increase in apparent viscosity for $\varphi_s \geq 0.65$. At T ≥ 550°C and $\varphi_s = 0.54$ the solid phase forms an almost entirely connected network composed of two alternating orientation domains. At T ≤ 550°C and $\varphi_s = 0.65$, intragranular fracturing and tensile fractures result from high local stresses at contact points between neighboring particles. The resulting bulk extensional fabric is almost parallel to the shortening direction.

1. Introduction

Magma transfer from a deep source to its final emplacement as an intrusion in the crust or lava after eruption at the surface is a mass and heat transport process that plays a major role in the chemical and physical differentiation of the Earth's lithosphere [e.g., Dingwell et al., 1993; Petford, 2003]. Magma is regarded as a multiphase system with varying content of three components: a silicate melt (the liquid phase), crystals (the solid phase) and bubbles (the vapor phase). As magma gradually cools and crystallizes during transfer, the chemical properties of the melt, the average shape, size distribution and shape distribution of the crystals, and the proportion and composition of the three different components progressively

change with considerable consequences for the rheological evolution of the magma [e.g., Dingwell et al., 1993]. Among these variables, crystal fraction (φ_s) and water content in the melt are considered as key parameters controlling the rheology of crystallizing magma [Petford, 2003]. The influence of water on the viscosity of hydrous silicic melts has been explored by many studies [e.g., Dingwell et al., 1996; Schulze et al., 1996]. Dingwell et al. [1996] have shown that the viscosity of haplogranitic melts decreases by several orders of magnitude in the presence of 0.5 wt % of water and continues to gradually decrease at higher water contents. By contrast, several rheological domains have been identified or proposed for magmatic suspensions during crystallization [Arzi, 1978; van der Molen and Paterson, 1979; Nicolas, 1992; Dingwell et al., 1993; Fernandez and Gasquet, 1994; Vigneresse et al., 1996]. These domains are separated by rheological and/or structural thresholds [Vigneresse et al., 1996; Rosenberg and Handy, 2005] whose limits in terms of solid fraction are vastly debated as they depend on many factors such as density and spatial organization of the solid phase [e.g., Saar et al., 2001; Rosenberg and Handy, 2005].

During the early stages of crystallization, silicate melt behaves as a Newtonian fluid. The dynamic viscosity of crystal-bearing melt increases regularly with crystal fraction and obeys the Einstein-Roscoe model [Roscoe, 1952]. For these low to moderate solid fractions, magma transfer processes involve bulk simple shear deformation in most geological settings. In this domain, homogeneous structures in the magma develop mostly by rigid body rotation of the suspended crystals [Fernandez et al., 1983; Ildefonse et al., 1992]. The rigid rotation of an ellipsoidal solid body immersed in a viscous fluid submitted to simple shear deformation has been described by Jeffery's [1922] model. During shearing, the orientation of the long axis a follows an orbit with a period that depends on the aspect ratio r = a/b of the particle, with b the minor axis. It is now accepted from experiments on analogue materials that natural particles with shape symmetries higher than monoclinic closely follow the rotation behavior of an ellipsoid having the same aspect ratio r [Willis, 1977; Arbaret et al., 2001]. Therefore numerical simulations based on Jeffery's equations can model the shape preferred orientations (SPO) development of a wide range of natural magmatic crystals with homogeneous shapes submitted to homogeneous simple shear [Fernandez et al., 1983; Ježek et al., 1994]. Such simulations have established the existence of a cyclic shape fabric, and the resulting model has been extensively applied to magmatic fabrics [e.g., Bouchez et al., 1997]. However, experiments on shape fabric development in sheared suspensions of 2-D and 3-D analogue materials have shown that this theoretical cyclic behavior is hardly respected in practice. First, rigid body rotation deviates from theory because of perturbation of the shear flow in between neighboring crystals [Ildefonse et al., 1992; Piazolo et al., 2002]. In addition, numerical simulations neglect possible contacts between crystals resulting from their relative motion during shearing. These mechanical interactions lead to the development of structural features such as transient tiling of crystals in viscous fluids with a solid fraction as low as $\varphi_s = 0.05$ [Fernandez et al., 1983; Arbaret et al., 1996], and stable clusters of particles for $\varphi_s > \sim 0.16$ [Ildefonse et al., 1992]. Another essential factor that may result in the stabilization of shape fabrics in simple shear is the shape distribution of the particle population. Analogue experiments [Arbaret et al., 1997; Fernandez and Fernandez-Catuxo, 1997] and numerical simulations [Ildefonse et al., 1997] have demonstrated that in simple shear a viscous fluid containing a population of particles with varying shapes develops steady state SPO at large strains. This fabric is typically characterized by a mineral foliation and lineation nearly parallel to the shear plane and shear direction of the flow, respectively [Arbaret et al., 1997]. Such results may also be expected for particle populations with lognormal shape distributions, as often found in natural igneous rocks [Bindeman, 2005]. This notion is fundamental for the shear flow determination in magmas from shape fabric distributions measured, for instance,

by classical optical microscopy or by anisotropy of magnetic susceptibility [Bouchez et al., 1997].

With increasing degree of crystallization, complex nonlinear rheologies develop. A rheological threshold defining a departure from Newtonian behavior has been proposed at $\varphi_s \sim 0.3–0.4$ [e.g., Fernandez and Gasquet, 1994; Lejeune and Richet, 1995; Saar et al., 2001; Bagdassarov and Pinkerton, 2004]. A linear viscoelastic (Bingham) rheology with the onset of a finite yield strength τ_c was measured at higher solid fractions [Pinkerton and Stevenson, 1992; Bagdassarov et al., 1994] and at the ductile-brittle (or glass) transition [Dingwell, 1997]. As deformation proceeds at these intermediate solid fractions, different microstructures develop in the magma that can in turn influence its rheology and possibly lead to strain localization. At large strains, SPOs of objects such as the crystals, septa, deformable enclaves or bubbles may develop homogeneously over the entire volume or change locally in orientation and intensity depending on the rheological properties of the magma. In turn, this structural evolution may affect the bulk rheological response of the magma. For instance, narrow shear zones resulting from strain localization by shear softening or local alignment of anisometric crystals forming S/C–like patterns at high solid fractions are two structures recognized to change the rheological behavior of the whole system [Nicolas, 1992]. In addition, the existence of a mechanism for oriented crystallization during shearing is still debated [Lofgren, 1980]. To investigate the interplay between the development of microstructures and rheology, large-strain experiments have typically been performed on monomineralic aggregates (e.g., calcite [Casey et al., 1998], olivine [Bystricky et al., 2000], quartz [Schmocker et al., 2003], magnesiowustite [Heidelbach et al., 2003]) and recently on bimineralic assemblages [Rybacki et al., 2003; Barnhoorn et al., 2005; Bystricky et al., 2006; Mecklenburgh et al., 2006] in a high-pressure and high-temperature gas-medium torsion apparatus [Paterson and Olgaard, 2000]. By contrast, most deformation experiments on partially molten rocks in the range $0.4 < \varphi_s < 0.8$ have been performed in compression and to low strains. These studies typically focused on the mechanical behavior of partially molten rocks ($\varphi_s > 0.54$) and the consequences for melt segregation and extraction [e.g., Arzi, 1978; van der Molen and Paterson, 1979; Paquet and François, 1980; Dell'Angelo and Tullis, 1988; Rutter and Neumann, 1995]. Only Paterson et al. [1998] and Petford [2003] with respect to plutonic rocks and Smith [2002] with respect to volcanic rocks have focused on the structural evolution of magmas during deformation to large strains by comparing field observations on fabrics and structures with existing rheological models.

In the late stages of crystallization, magmatic rocks are thought to undergo a transition from liquid to solid-like behavior that is associated with a large increase in viscosity of up to 4 orders of magnitude [Rosenberg and Handy, 2005]. Across this transition, the magma evolves from a viscous suspension whose rheology is controlled by the liquid, to an interconnected framework capable of transmitting deviatoric stresses [Petford and Koenders, 2001; Petford, 2003; Stickel and Powell, 2005]. In his pioneering work, Arzi [1978] observed this threshold at crystal fractions of $\varphi_s \sim 0.8$, and defined it as the Rheological Critical Melt Percentage (RCMP). In later experimental studies, a similar transition was estimated at various crystal fractions between 0.4 and 0.9 [e.g., van der Molen and Paterson, 1979; Lejeune and Richet, 1995]. Along the same lines, a Particle Locking Threshold (PLT) was defined at about $0.7 < \varphi_s < 0.9$ by Vigneresse et al. [1996]. Determining a precise value of the RCMP experimentally is difficult because it requires experiments on a well-controlled system over a large range of crystal fractions. As a result, the RCMP is still debated. The RCMP may in fact vary depending on melt viscosity, and shape, size distribution, and SPO of the solid fraction [Dingwell et al., 1993; Saar et al., 2001]. Finally, an additional threshold called melt

connectivity transition (MCT) was defined at $\varphi_s > \sim 0.93$ by Rosenberg and Handy [2005], on the basis of their review of existing experimental data. This transition is characterized by an even greater viscosity contrast than the RCMP and may be due to the breakdown of melt interconnectivity, without any fundamental changes in the structure of the solid aggregate.

Partially molten granitic rocks were deformed at different solid fractions either by adding water at constant temperature [van der Molen and Paterson, 1979] or by increasing temperature [Rutter and Neumann, 1995]. An attempt to control melt fraction, composition and water content independently was made on synthetic aggregates of granitic composition [Mecklenburgh and Rutter, 2003]. Compression experiments were also performed on synthetic olivine aggregates in the presence of basaltic melt [e.g., Hirth and Kohlstedt, 1995a, 1995b] and on a partially molten lherzolite [Zimmerman and Kohlstedt, 2004]. Most such studies focused on measuring rheologies rather than on characterizing microstructures, with the exception of studies concentrating on melt topology in olivine melt samples ($\varphi_s > 0.8$) deformed in compression [e.g., Daines and Kohlstedt, 1997; Scott and Kohlstedt, 2006] or in shear using a diagonal-cut assembly [Holtzman et al., 2003, 2005; Katz et al., 2006].

Overall, the viscosity of a crystallizing magma increases by as much as 14 orders of magnitude over its full range of crystallization ($0 < \varphi_s < 1$), with many rheological thresholds that are still poorly constrained [Rosenberg and Handy, 2005]. Surprisingly little attention has been paid to the structures of experimentally deformed magmas, even though constraining the relationship between characteristic magmatic microstructures and the rheological behavior of magma over the entire range of crystallinity is fundamental to be able to model magma transfer processes and determine the rheological history of magmatic bodies from the observation of their preserved structures. In this contribution, we present our results on the development of microstructures in experimentally deformed magmatic suspensions. In order to focus on the effect of solid fraction on rheology and structural development, we have synthesized samples composed of a water-undersaturated aluminosilicate melt and various solid fractions of crushed alumina grains ($0.00 < \varphi_s < 0.76$). These crystal melt mixtures were deformed in torsion at high pressure and high temperature in a Paterson gas-medium apparatus and deformed samples were analyzed by image analysis on polished sections. Particular attention was paid to the relationships between rheology measured during the deformation experiments and resulting microstructures, including shape fabrics of crystals and bubbles (when present), local SPO bands, and other microstructural heterogeneities resulting from strain localization in narrow zones. The results are discussed and compared with previous experiments on analogue materials and natural partially crystallized melts, and with numerical simulations. A general description is proposed for the rheological evolution of a crystallizing magma that links the development of characteristic microstructures in magmatic suspensions with changes in rheological behavior and in flow law parameters as a function of crystal fraction for $0.00 < \varphi_s < 0.76$.

2. Experimental Procedure

2.1. Sample Synthesis and Hydration Technique

[8] A single synthetic aluminosilicate melt was chosen for all experiments, in order to focus entirely on the effect of solid fraction on the deformation properties of a partially crystallized magma. A dry glass was synthesized by Schott AG, Germany, and has a haplogranitic composition (SiO_2 = 78.8, Al_2O_3 = 12.4, Na_2O = 4.6 and K_2O = 4.2%, as measured by microprobe analysis [Champallier et al., 2007]) close to the so-called HPG8 composition of

Holtz et al. [1992]. This composition was selected because its rheology and water solubility at our experimental conditions are well known [Holtz et al., 1992; Schulze et al., 1996; Dingwell et al., 1996]. The dry glass was crushed and the resulting powder (grain diameter Ø < 20 μm) was mixed with a solid phase consisting of crushed alumina crystals with a sieved fraction of 45 μm < Ø < 90 μm. Alumina was chosen to avoid any crystallization/dissolution and hydration of the grains during the timescale of the torsion experiments (≤12 hours), thus ensuring constant composition, solid fraction and water content within the melt during deformation [Martel et al., 2001]. Five mixtures were prepared with different solid fractions φ_s, namely, 0.16, 0.34, 0.54, 0.65 and 0.76 (Figure 1). The glass/solid mixtures were loaded with distilled water in a gold capsule (20 mm in diameter and 30 to 35 mm in length). The amount of added water was calculated to obtain 2.5 wt % in the melt, independently of solid fraction. As a reference, a hydrated crystal-free melt was prepared with the same procedure. The five HPG suspensions and the crystal-free hydrated glass were melted at 100 MPa and 1000°C for a minimum of 1 month, i.e., long enough to ensure homogenization of the water in the melt. The water content in synthesized samples was measured by FTIR and Karl Fisher Titration and is detailed by Champallier et al. [2007].

2.2. Deformation Experiments

[9] High-temperature high-pressure torsion experiments were performed in an internally heated gas-medium deformation apparatus (Paterson instrument, Australian Scientific Instruments) at ETH Zurich. The experimental setup and techniques are described in detail by Paterson and Olgaard [2000]. Torsion experiments allow deformation to large strains in a geometry resembling simple shear and the determination of mechanical data as a function of strain under constant bulk strain rate.

[10] Cylindrical samples 11.8 to 14.9 mm in diameter, 5.0 to 11.5 mm in length, and with ends parallel to within 3 μm were cored and machined from the synthesized material. During deformation, each sample was held between alumina pistons and jacketed in copper. In two experiments at very high temperature, iron was used as jacketing material instead of copper. An inner sleeve consisting of a 25 μm thick platinum foil was always wrapped around the specimen to avoid any chemical reaction between melt and copper (or iron), and limit water loss during the experiment. Microprobe analyses on deformed samples show that water loss from the samples is negligible [Champallier, 2005]. All experiments were conducted at a confining pressure of 300 MPa and temperatures ranging from 475°C to 900°C using the torsional configuration [Paterson and Olgaard, 2000]. Frequent temperature calibrations ensured thermal gradients within the samples of <1°C cm^{-1}. Samples were deformed at constant angular displacement rates corresponding to constant strain rates between 2.0×10^{-5} and 2.1×10^{-3} s^{-1} at the outer radii of the cylinders. The angular displacement rate was either held constant throughout the experiment, or was changed in steps in order to get additional mechanical data. Angular displacement was recorded with an external RVDT and torque was measured with an internal capacitance load cell with a resolution of 0.2 Nm. The procedure to calculate shear stress from measured torque is detailed by Paterson and Olgaard [2000].

[11] Before calculation of the shear stress, the measured torque was corrected for the strength of the copper jacket surrounding each sample. Torsion deformation tests were conducted on copper samples with the same composition as the jacket to determine its strength at the experimental conditions. Copper data were in good agreement with flow laws for copper compiled by Frost and Ashby [1982]. In most stepping tests, the resulting jacket corrections were on the order of 5–30% of the total torque recorded during the tests. In a few

steps at the highest temperatures and lowest shear rates, the apparent viscosities of the samples could not be determined because of a high contribution of the copper jacket to measured torque. Analysis of the mechanical data is presented in detail by Champallier et al. [2007]. Experimental conditions and rheological data are summarized in Tables 1 and 2, respectively.

2.3. Analytical Techniques and Particle Shape Properties

Polished thin sections were prepared from deformed samples parallel to the [XZ] plane (with X the direction of shear, and Z the normal to the [XY] plane of shear), close to the outer surface of the samples. In this plane, deformation occurs approximately by simple shear. The finite strain γ_{sec} in this section of observation is slightly lower than the finite strain γ measured at the maximum sample radius. Microstructural observations and sectional shape fabric measurements were performed on both optical microscope and scanning electron microscope (SEM) images (microstructural analyses are summarized in Table 3). SPO of the solid alumina and the bubble phases were obtained by applying two methods depending on the concentration of objects. First, for solid fractions $\varphi_s \leq 0.34$, grains are distinguishable and separated from each other. In that case, the two-dimensional shape properties of each type of object, alumina grains and bubbles, were determined by applying the inertia tensor method using the program SPO.EXE [Launeau and Cruden, 1998; Launeau, 2004]. The shape fabric of the alumina grain population is obtained by averaging the single object inertia tensors and the one for the bubble population by using the Rf/Phi method [Lisle, 1985]. Second, for $\varphi_s \geq 0.54$, alumina grains form an interconnected network in which objects cannot be separated easily from each other by image processing on 2-D polished sections (Figure 1). Therefore the overall shape fabric was calculated by using the intercept method applied to the whole image [Launeau and Robin, 1996]. The method involves a Fourier series decomposition of the polar plot of intercepts, and yields a rose of directions which quantifies the fabric symmetry, its direction α ($-90° < \alpha < 90°$, positive for a clockwise orientation with respect to the dextral shear direction $\alpha = 0$), and its intensity expressed by the axial ratio R [Saltikov, 1958; Launeau et al., 1990; Launeau and Robin, 1996]. In these highly concentrated suspensions, bubble shapes were not analyzed because they cannot be distinguished from the trace of alumina grains plucked during the polishing procedure (Figure 1, $\varphi_s = 0.54$, 0.65 and 0.76).

2.4. Characterization of the Starting Material

[13] In the starting material, the fraction of residual bubbles preserved after sample hydration is $\varphi_b = 0.01$, as measured on polished sections of crystal-free melt (HPG10, Figure 1). The average surface based on 1001 bubble measurements is 147.56 ± 96.53 μm^2, which corresponds to an idealized mean bubble diameter of 13.7 μm. The axial ratios r = a/b have approximately a lognormal distribution with an average axial ratio $R = 1.17 \pm 0.16$ reasonably close to an ideal spherical object (i.e., R = 1.00, Figure 2). Shape properties of the bubble population were also determined in the starting material containing 16% of alumina grains (HPG5, Figure 2a). The mean bubble diameter of 13.9 μm is close to the one obtained for crystal-free melt. The lognormally distributed axial ratios exhibit an average of $R = 1.55 \pm 0.8$ with a significant dispersion toward large aspect ratios, with a maximum of r = 5.8. These large aspect ratios are measured on bubbles in contact with or more likely squeezed between alumina grains, while isolated bubbles conserve an isotropic shape (Figure 1, $\varphi_s = 0.16$).

Because of the crushing procedure, some of the alumina grains display strong concavities and convexities (Figure 1). The potential influence of these complex shapes on rheology and

shape fabric development in the magmatic suspensions will be detailed in the Discussion. In the starting material with $\varphi_s = 0.16$ (HPG5, Figure 2), grain axial ratios exhibit a lognormal distribution (with R = 2.35 ± 1.14) comparable to those commonly measured in magmatic, idiomorphic and even fragmented crystal populations [Bindeman, 2005]. For $\varphi_s > 0.34$, intragranular fracturing is recognized, suggesting high local stresses at contact points between neighboring particles of the solid framework (Figure 1). The percentage of split grains has not been quantified, but clearly increases with increasing solid fraction. The volume fraction of the solid phase was controlled by measuring the area percentage of alumina grains on polished sections of the synthesized materials. The results yield a regression line constrained through the origin with a slope of 0.83 that links volume percentage of alumina grains mixed with the melt during sample preparation and alumina surface percentage on 2-D sections (Figure 2b). For $\varphi_s = 0.65$, the surface percentage appears overestimated. At this concentration, melt forms thin films between crystals, for instance between fragments of split grains (typically less than 2 pixels at the used resolution). During segmentation of the analyzed images, these thin melt films are not fully distinguished from the solid phase, which is therefore overestimated. In all the starting materials, alumina grains are not preferentially oriented, confirming nearly isotropic pressure conditions during synthesis as already suggested by the bubble shape analysis in crystal-free melt.

Ten samples with solid fractions φ_s between 0.0 and 0.76 were deformed at different temperatures and strain rates to total shear strains of up to 21.3 (Table 1 and Figure 3). Typically, experimental conditions (temperature and shear strain rate at the outer diameter of the sample) were held constant over small strain intervals of ~0.6–1.2 or were kept constant up to very large strains in order to measure the evolution of strength as a function of strain (Figure 4a). The mechanical data are briefly presented below and are treated in detail by Champallier et al. [2007].

At low solid fractions ($\varphi_s < 0.34$), bulk deformation remains perfectly homogeneous (e.g., PO540 and PO514, Figure 3), and the mechanical data indicate steady state behavior irrespectively of finite strain (e.g., PO540 and PO519, Figure 4a). At higher solid fractions, pronounced grooves on the outside jacketing material and asymmetric shapes of the deformed samples denote increasingly heterogeneous bulk deformation with increasing solid fraction (e.g., PO609 and PO528, Figure 3). Progressive strain hardening occurs in these samples (PO524, Figure 4a), especially at faster strain rates.

The magmatic suspensions strengthen with increasing crystal content, as illustrated by Figures 4a and 4b. No reliable mechanical data were obtained for $\varphi_s = 0.76$, as deformation was limited to a very small total strain ($\gamma \sim 0.05$, PO515 in Figure 3) because of technical problems caused by the very high strength of the material. In addition, Figure 4b shows that the rheology becomes non-Newtonian at higher solid fractions. Non-Newtonian behavior may be described by a power law equation of the form typically used to model high-temperature creep of rocks:

$$\dot{\gamma} = A\tau^n \exp(-Q/RT) \qquad (1)$$

where $\dot{\gamma}$ is shear strain rate, τ is shear stress, T is temperature (K), R is the gas constant, and A, n and Q are empirical parameters called respectively the preexponential term, the stress exponent and the activation energy for creep [e.g., Poirier, 1985]. The stress exponent n (corresponding to the slope to the data on a logarithmic plot of stress versus strain rate, e.g., Figure 4b) is equal to 1 for Newtonian creep and is greater than 1 for materials undergoing

shear thinning. For each crystal fraction (φ_s = constant), we fit equation (1) to the rheological data by a nonlinear least squares regression procedure. This analysis yielded flow laws with stress exponents n increasing with crystal fraction from 1 to ~3, and activation energies Q in the range of 210 to 250 kJ mol^{-1}. Since such variations in activation energies were not significant (all values being within one standard deviation), new fits were done to the data for each composition using a constant overall activation energy Q_{av}, where Q_{av} = 231 ± 19 kJ mol^{-1} is the weighted average of the individual activation energies (Figure 4c). Table 2 lists the rheological parameters determined using this approach.

Figure 5 summarizes the rheological behavior of the magmatic suspensions with solid fractions φ_s between 0 and 0.65. In the case of a non-Newtonian rheology, viscosity is dependent not only on crystal fraction and temperature but also on strain rate (or stress). Therefore, for comparison all the experimental data were plotted as apparent viscosity as a function of crystal fraction after normalization to a constant strain rate. Flow is Newtonian (n = 1) for φ_s = 0.0–0.16 and deviation from Newtonian behavior (n > 1) is observed for crystal fractions of approximately φ_s > 0.2. The apparent viscosity increases by 2.5 orders of magnitude between φ_s = 0.34 and 0.65 and extrapolation of the data suggests a very sharp increase in viscosity for $\varphi_s \geq 0.65$.

3.2. Shape Fabric of the Bubble Phase

Although measuring the SPO of deformable particles during shearing was not within the initial scope of this study, the presence of residual bubbles in crystal-free (φ_s = 0) and in φ_s = 0.16 samples provided the opportunity to test the potential use of such deformable objects as strain markers in haplogranitic melts deformed at high pressure and temperature.

3.2.1. Bubbles in Crystal-Free Samples (φ_s = 0.00)

The initially nearly spherical bubbles (with a mean diameter of 13.7 μm, HPG10 in Figure 1) appear elongated in [XZ] sections of crystal free melt deformed to a finite strain γ_{sec} = 7.5 (PO540, Figure 6). SPO measurements by the single object inertia tensor method on 1001 bubbles yield a shape fabric orientation α = −8.87° and an axial ratio R = 7.09 (sign convention for α in Figure 7). On the basis of the observation of strongly deformed bubbles (white arrow in Figure 6), a first assumption is to consider that the bubbles deform perfectly during steady state shear deformation, i.e., the bubbles behave likes “passive markers” with no apparent viscosity contrast between them and the melt. In that case, theoretical relationships between α, R and finite shear strain γ can be determined by using the finite strain ellipse theory [Ramsay and Graham, 1970]. The relationship between the theoretical long axis orientation α and the applied finite strain γ is derived from the March [1932] equation:

$$\alpha = \frac{1}{2}\arctan\frac{2}{\gamma} \qquad (2)$$

and R is equal to the aspect ratio of the strain ellipse expressed in terms of the quadratic extensions λ_1 and λ_2:

$$R = \left(\frac{\lambda_1}{\lambda_2}\right)^{\frac{1}{2}} \qquad (3)$$

with [Ramsay, 1967, equations (2)–(7), p. 30]:

$$\lambda_{(1,2)} = \frac{1}{2}\left[\left(\gamma^2 + 2\right) \pm \gamma\left(\gamma^2 + 4\right)^{\frac{1}{2}}\right] \qquad (4)$$

For a finite strain $\gamma_{sec} = 7.5$, equations (2), (3), and (4) yield a theoretical orientation of the long axis of a passive marker of $\alpha_{th} = -7.46°$ and a theoretical aspect ratio of $R_{th} = 58.2$. While α_{th} is close to the value $\alpha = -8.87°$ determined for the bubble population, R_{th} is much larger than the average R = 7.09 obtained for the bubble population and even far from the aspect ratio r = 21.2 of the most elongated bubble measured (Figures 6 and 7).

3.2.2. Bubbles in Crystal-Bearing Samples ($\varphi_s = 0.16$)

Three experiments (PO514, PO610 and PO519) were performed on samples with $\varphi_s = 0.16$ to different finite strains ($\gamma = 2.5$, 6.1 and 17.5 respectively). As in crystal-free melt, a residual phase formed of dispersed spherical bubbles (with a diameter of 13.9 μm) is present in the starting material HPG5 (Figure 1). The shape fabric orientation α is −24° for $\gamma_{sec} = 2.2$ and stabilizes at about −16° to −17° for higher finite strains (Figure 8). Intensity of the bubble shape fabric ranges from R = 1.38 to 2.24. The lowest value is recorded in PO610, where a significant number of alumina grains were plucked during polishing, leaving black irregular areas in the images (Figure 8). Although we tried to manually suppress the largest areas, residual traces of plucked grains incorporated to the bubble phase during the segmentation process likely contributed to an underestimation of the value of R (Figure 8).

In Figure 9, the shape fabric orientations α for $\varphi_s = 0$ and $\varphi_s = 0.16$ are compared to the orientations predicted by the March [1932] model. For the $\varphi_s = 0.16$ runs, α departs from the model as early as $\gamma_{sec} = 2.2$ and is stable at large finite strains. In addition, the intensity R measured in PO610 is much lower than those measured in PO540 ($\varphi_s = 0$) for similar finite strains (Figure 8). All evidence points to a strong influence of the solid fraction on the shape fabric acquired by the bubble phase.

3.2.3. Residual Bubbles as Potential Strain Markers

In experiment PO540 ($\varphi_s = 0.0$, $\gamma_{sec} = 7.5$), the shape fabric orientation α of the residual bubble population fits with the theoretical orientation given for perfectly deformable bubbles in a steady state shear flow to a finite strain $\gamma = 7.5$. This implies that the interfacial tension forces that tend to maintain - or restore - the initial sphericity of the bubbles are negligible compared to the viscous forces that cause deformation of the bubbles [Stein and Spera, 1992, 2002; Llewellin and Manga, 2005]. By contrast, measured bubble aspect ratios r are all much lower than the theoretical value of $R_{th} = 58.2$ (Figure 7a). In turn, this suggests that the interfacial forces play a significant role in limiting deformation of the bubbles. To answer this apparent discrepancy, we estimated the capillary number Ca expressing the ratio between viscous forces and interfacial tension forces [Manga et al., 1998]:

$$Ca = \frac{l\eta\dot{\gamma}}{\kappa} \qquad (5)$$

where κ is surface tension, l is the mean undeformed bubble radius and η is melt viscosity. Liquid-bubble interfacial tension has not been measured in a water-undersaturated

haplogranitic melt at the temperature and pressure conditions of our deformation experiments. However, surface tension can be approximated from the measurements of Bagdassarov et al. [2000] at 1 bar and nearly dry conditions. For the minimum temperature of 475°C, the best fit expression of Bagdassarov et al. [2000] yields a surface tension $\kappa = 240$ mN m^{-1}, which is close to the value of 250 mN m^{-1} deduced by Llewellin and Manga [2005] from Murase and McBirney [1973]. Taking this last value for κ, a measured mean bubble radius of 5.8 μm and a melt viscosity of $1 \times 10^{10.3}$ Pa s as measured in the PO540 experiment, the capillary number ranges from a minimum of Ca = 93 for $\dot{\gamma} = 2.01 \times 10^{-4}$ s^{-1} to a maximum of Ca = 289 for $\dot{\gamma} = 6.24 \times 10^{-4}$ s^{-1}. Such Ca $\gg 1$ confirms that interfacial forces are negligible against viscous forces. Therefore bubbles should deform perfectly and remain deformed during cooling and relaxation, following the March model of perfectly deformable inclusions in simple sheared suspensions [March, 1932; Hinch and Acrivos, 1980] (Figure 9, $\varphi_s = 0.0$). The size and morphology of bubbles observed on analyzed SEM images provide more arguments to explain the discrepancy between measured axial ratios and orientations and the values predicted by the March [1932] model. If shear stresses overcome capillary forces, bubbles may fragment at large strains and high strain rates into smaller, nearly isotropic or at least less elongated, bubbles [Stein and Spera, 1992]. In our experiments, some of the bubbles display this boudinage-like morphology invoked by Stein and Spera [1992] (black arrow in Figure 6). The smallest bubbles that result from the boudinage (about d < 10 μm) yield nearly random, distributed orientations α which do not significantly affect the mean orientation of the bubble population controlled by the largest preserved bubbles (Figure 7). In addition, fracturing and breaking up of small glass pieces along bubble edges during the polishing process also likely affect the aspect ratio of segmented bubbles (Figure 6). However, as for the boudinage-like fragmentation, it does not significantly affect the long axis orientation α of strongly deformed bubbles. Thus both fracturing during polishing and boudinage-like fragmentation do not affect α but affect R. Consequently, residual bubbles can be used as strain markers for this melt composition at our experimental conditions, and the finite strain γ can be calculated from the average long axis orientation α of the bubbles.

3.3. Shape Fabric of the Crystal Fraction

As detailed in the experimental procedure, for $\varphi_s \leq 0.34$ each particle can be separated and analyzed individually in segmented images. Conversely, for $\varphi_s > 0.34$ the crystals form a continuous network and cannot be separated from each other. For these crystal fractions, the orientation α and the intensity R of the SPO were measured locally in order to quantify possible SPO variations over the [XZ] section. Segmented images were divided in 378 × 378 pixels subimages for local analysis following a diamond-shaped grid (Table 3). The local orientations α of the shape fabric measured in subimages are represented by arrows at the subimage centers and placed on top of intensity R maps calculated by kriging (see Figure 10 for illustration).

3.3.1. Samples With $\varphi_s = 0.16$

Three experiments (PO514, PO610 and PO519) were performed to different maximum finite strains ($\gamma = 2.6$, 7.0 and 17.5, respectively) at the outer radii of the samples, corresponding to strains of $\gamma_{sec} = 2.2$, 6.1 and 15.0, respectively, in the analyzed [XZ] sections (Figure 8). Grain shape fabric orientations α are close to the shear direction X independently from finite strain ($\alpha = -2.2°$, $-1.7°$ and $-6.3°$ at $\gamma_{sec} = 2.2$, 6.1 and 15.0, respectively; sign convention for α in Figure 7). Rose diagrams of the orientations of the single object inertia tensor yield comparable average orientations and show a unimodal distribution that widens with

increasing strain (Figure 8). This decrease in shape fabric intensity with strain is also evidenced by the decrease in axial ratio of the mean tensor ellipse from R = 1.48 at γ_{sec} = 2.2 to R = 1.29 at γ_{sec} = 15.0.

3.3.2. Samples With Φ_s = 0.34

A sample with Φ_s = 0.34 was deformed to a strain γ = 8.5 (PO609, γ_{sec} = 7.5, Figure 10). The surface of the sample is affected by a number of small spiral grooves that suggest heterogeneous deformation (Figure 3). The local shape fabric orientations α measured on subimages and placed on R maps are heterogeneous (Figure 10). The rose diagram of orientations α indicates a slightly bimodal distribution, with the main orientation nearly parallel to the X direction of shear and a less pronounced second orientation at −30° from X (Figure 11). The average orientation $\alpha = -6.8° \pm 30.2°$ is close to the value calculated by the intercept method applied to the whole image ($\alpha = -5.69°$). The intensities R obtained on subimages vary from 1.1 to 1.48 and follow a unimodal distribution. The average intensity determined by the intercept method (R = 1.12, Figure 11) is much lower than that measured for Φ_s = 0.16 (R = 1.32 for a similar finite strain of 6.1; PO610, Figure 8).

The R map provides evidence of distinct areas with either R < 1.2 or R > 1.2 that form alternating bands oriented at about −40° with respect to the direction of dextral shear (Figure 10b). Although it cannot be excluded that the orientation and the average width (~200 μm) of these alternating bands are partly influenced by the diamond-shaped grid of the analyzed subimages, the effect of the grid shape on the average measurements is likely minor, as shown by a study on natural deformed gabbros that used a similar methodology [Arbaret and Burg, 2003]. In addition, there is no apparent link between these bands and the areas formed by the two orientations evidenced by the rose diagram (Figures 10 and 11).

3.3.3. Samples With Φ_s = 0.54

Three experiments (PO524, PO516 and PO528) were performed to different maximum finite strains (γ = 8.8, 10.8 and 21.3, respectively) at the outer radii of the samples, corresponding to finite strains of γ_{sec} = 7.5, 9.5 and 18.9, respectively, in the [XZ] sections (Figure 12). The outer surfaces of the samples show heterogeneous bulk deformation (Figure 3). For instance, PO528 is affected by a single spiral groove where the sample radius is reduced by 800 μm. Analysis of SEM images indicates two types of microstructures in these samples. In PO516 and PO528, the grain size distribution is similar to the one observed before deformation in the starting material HPG6 (Figures 12 and 1). At such high solid fractions, neighboring grains in contact with each other in the solid framework cannot accommodate all the local stresses by solid rotation or sliding, resulting in some intragranular fracturing (Figures 12 and 13). In PO516, PO528 and HPG6, intragranular fracturing is present in the same proportion and thus likely results from local stress accommodation during sample synthesis. By contrast, PO524 is characterized by a very different texture (Figure 12). A large number of grains are fractured in a multitude of small angular pieces, except for rare porphyroclast-like preserved grains (Figure 14a). In some areas, local deformation was low enough after the fracturing event to preserve the original shape of the fractured grains, highlighting the importance and pervasiveness of intragranular fracturing in this sample (Figure 14c). The texture observed in PO524 expresses a cataclastic behavior, a process that apparently remained limited in PO516 and PO528.

Differences in textures are correlated with differences in shape fabrics measured in the three runs. For PO516 and PO528, the shape fabric orientations α measured on whole images are close to the shear direction (α = 3.01° and α = −5.29°, respectively, Figure 11). The arithmetic mean shape fabric orientations α of the measurements made on subimages are close to these values for both experiments; the largest deviation of Δα = 14.7° is found for PO528. For PO516 (γ_{sec} = 9.5), the rose diagram of the shape fabric orientations α shows a bimodal distribution that is nearly symmetric with respect to the shear direction X. For PO528 (γ_{sec} = 18.9), the bimodal distribution for α is less evident, because of a large distribution in the corresponding rose diagram. By contrast, the shape fabric in the sample characterized by a cataclastic texture (PO524) departs strongly from the one in PO516 and PO528 (Figure 11), with α = 32.06° for the whole image and α = 23.6° ± 27.8° as average of the subimages. For all three samples PO516, PO528 and PO524, the intensities R measured on whole images (R = 1.05, R = 1.04 and R = 1.03, respectively) and on subimages (bimodal distribution with an average of R = 1.07 ± 0.04 and R = 1.05 ± 0.03 for PO516 and PO528; and unimodal distribution with R = 1.05 ± 1.02 for PO524) are all low compared to the ones measured for lower solid fractions (R = 1.2 for φ_s = 0.16 in Figure 8 and R = 1.12 for φ_s = 0.34, PO609 in Figure 11).

In R maps for PO516 and PO528, areas with R < 1.06 form bands oriented at about ±30° with respect to X (Figure 12). As already pointed out for the φ_s = 0.34 experiment, it cannot be excluded that the measured orientation of the bands is partly influenced by the diamond shape of the sampling grid of the subimages during the kriging calculation. The local shape fabric orientations α in PO516 and PO528 give clear evidence of a bimodal distribution composed of areas with positive orientations alternating with areas with negative orientations (white and black arrows, respectively, in Figure 12). In sample PO524 characterized by an apparent cataclastic texture, a major overall shape fabric orientation lies at α ~ + 24° from the direction of shear X (Figures 11 and 12, sign convention in Figure 7), except for one area where an angle of α ~ −60° is associated with preserved porphyroclasts (Figure 14a). This orientation corresponds to the orientation of a 200 μm thick shear zone whose top to the right sense of shear is given by the deflection of the matrix around the rotating porphyroclasts (Figures 14a and 14d). On the basis of the black traces of plucked disaggregated or fractured grains in the segmented images (PO 524, Figure 12), other small shear zones with similar orientations are suspected to exist in the section. However, they are not evidenced by shape fabric analysis, as they affect only a limited number of grains with respect to the size of the analyzed images.

3.3.4. Samples With φ_s = 0.65

A sample with φ_s = 0.65 was deformed to a finite strain γ = 7 (PO612, γ_{sec} = 3.3, Figures 13 and 14). The shape fabric orientations α on the [XZ] section are remarkably regular with an average of 67.8 ± 7.5° from the shear direction (rose diagram in Figure 11). Contrary to all other experiments with lower solid fractions, there are no associated negative orientations. The shape fabric intensity yields a unimodal distribution with an average R = 1.10 ± 0.03, slightly higher than intensities measured for φ_s = 0.54.

3.3.5. Samples With φ_s = 0.76

Owing to technical difficulties, the sample with the highest solid fraction (φ_s = 0.76) was deformed only to a strain of γ ~ 0.05 (PO515, Figure 3). No structures developed in the sample at such small finite strain.

4. Discussion

4.1. Constraints on Application of Experimental Results

The experiments in this study were designed to explore the effect of solid fraction on the rheology and the structural evolution of magmatic suspensions during noncoaxial deformation at high pressure and temperature. For this reason, we chose a model system consisting of a single synthetic aluminosilicate melt with a fixed water concentration mixed with varying solid fractions of crushed alumina grains. It is evident that such a simplified system, deformed at temperatures and strain rates limited by our experimental setup, may not necessarily reproduce all conditions and processes in magmatic settings ranging from the slow cooling of deeply emplaced plutons to fast volcanic flows. In crystallizing magmas, the residual melt fraction evolves continuously toward silicic compositions with, among other components, enrichment of water content that gradually decreases the viscosity of the melt phase. This decrease in melt viscosity may balance or even exceed the effect of progressive crystallization of anhydrous mafic and calc-alkaline phases on bulk viscosity [Scaillet et al., 1997; Petford, 2003]. An extreme case is illustrated by dacitic compositions where bulk viscosity can decrease at large crystallinities [Scaillet et al., 1998]. Consequently, the rheology of cooling magmas over their liquidus-solidus domain may in some cases differ from the one measured in the present study on magmatic suspensions with a fixed melt composition and water content. The Einstein-Roscoe equations [Roscoe, 1952] have often been used to model the rheological behavior of crystallizing magmas. As these equations consider only the effect of solid-phase content on the viscosity of particle-bearing fluids, they may not always be adequate to model the behavior of magmas with large crystallinities (larger than about 0.5) and have spurred the development of empirical rheological models [e.g., Rosenberg and Handy, 2005; Costa, 2005]. While the rheological behavior of the magmatic suspensions deformed in this study may not reproduce all of the complexities found in nature, it may help in developing and constraining rheological models of crystallizing magmatic rocks.

The initial alumina grain population in our samples exhibits a log normal size distribution almost representative of magmatic crystal populations [Bindeman, 2005]. However, the shape of the grains is irregular, with concave to convex faces and complex angular relationships, far from idiomorphic crystal shapes irrespective of any crystallographic system. Analogue 3-D experiments carried out on the rotational behavior of parallelepipedic particles embedded in a viscous matrix submitted to simple shear deformation showed that such particles behave as ellipsoidal objects having the same aspect ratio [Arbaret et al., 2001]. This behavior is explained by a certain volume of the viscous matrix that remains undeformed around the particle, the solid particle-undeformed matrix couple behaving as a uniform solid object. Therefore we believe that the complex shapes of the crushed grains used in our experiments have little or no influence on their rotational behavior and by extension on the shape fabric acquisition in the low to medium solid fraction range. This is not true at high solid fractions, where grain shape plays a direct role in interactions and contacts between grains and their rearrangement by solid rotation and slip between neighboring tabular grains [Ildefonse et al., 1992; Nicolas, 1992]. In addition, the existence at high solid fractions of a solid framework composed of less anisometric particles causes intragranular fracturing during deformation, resulting in dilatant and shear hardening processes [Smith, 1997; Petford and Koenders, 2001].

All runs were conducted at subsolidus temperatures from 475°C to 600°C and strain rates from 2.0×10^{-5} s^{-1} to 2.1×10^{-3} s^{-1}. These conditions were constrained by the capabilities of the Paterson apparatus to measure the torque needed to deform the sample in response to applied strain rate during stepping tests. An additional constraint was to choose conditions far enough from the ductile to brittle (glass) transition of the melt, to ensure that all experiments remained in the ductile field. This condition is essential at $\varphi_s > \sim 0.5$, where intragranular fracturing-related fabrics and strain localization may develop. The glass transition of the melt as a function of water content is predicted by the empirical equation proposed by Dingwell [1998]:

$$T_g = 786 - 83.47 \ln(C_{H2O})$$

where T_g is the glass transition at the $\log_{10}$ (Pa s) = 12.38 isokom and C_{H2O} the water concentration in wt %. For a water concentration of 2.5% in the melt, the equation yields T_g = 436.5°C, or a difference of ΔT = 38.5°C with the lowest temperature of 475°C reached during the experiments. In addition, the viscosity of $\log_{10}$ (Pa s) = 10.87 measured at this temperature is much lower than the predicted viscosity at the glass transition. These differences in both temperature and viscosity confirm that the experiments were performed above the glass transition.

Finally, the explored strain rate range is far from representative of deeply emplaced magmas where expected strain rates are generally about 10^{-10} s^{-1} [Petford, 2003]. However, the fast strain rates reached in our experiments at subsolidus temperatures are relevant for silicic magmas emplaced at shallow depths in subvolcanic dykes and sills or erupting at the surface to form domes and lava flows (10^{-3} to 10^{-7} s^{-1} [Chadwick et al., 1988; Spera et al., 1988]). Keeping all these limitations in mind, a general evolution of structures and rheology of crystallizing magmas is proposed.

4.2. Evolution of Rheology With Crystal Fraction

At low crystal fractions (φ_s = 0.0 to 0.16), where interaction between rotating porphyroclasts is very limited, deformation is Newtonian and a mild increase in viscosity with crystal fraction is well approximated by the Einstein-Roscoe equation (see Champallier et al. [2007] for a detailed discussion). Deformation deviates from Newtonian to pseudoplastic flow ($n > 1$) at intermediate crystal fractions ($0.16 \leq \varphi_s \leq 0.34$) because of an increase in tortuosity of the fluid as colliding clasts create clusters in the suspension. At crystal fractions ≥ 0.54, strong cataclastic textures develop. Clasts form a solid framework and produce shear bands and S/C structures. Consequently, the suspension undergoes strain hardening and deformation is increasingly heterogeneous. Shear thinning is accentuated ($n \sim 2$ to 3) and the increase in apparent viscosity becomes more pronounced with crystal content. Previous results on crystal-bearing silicate melts have shown an abrupt transition from Newtonian to non-Newtonian flow and an increase in apparent viscosity of up to 6 orders of magnitude at $\varphi_s \sim 0.40$ [Lejeune and Richet, 1995]. By contrast, here the apparent viscosity increases by ~2.5 orders of magnitude for a change in crystal fraction from φ_s = 0.0 to 0.54, and by ~1.5 orders of magnitude between φ_s = 0.54 and 0.65. Extrapolation of the experimental data to high solid fractions suggests a rheological threshold for these magmatic suspensions at around φ_s = 0.60–0.75.

4.3. Newtonian Field at Low Solid Fraction ($\varphi_s \leq 0.16$)

Pure hydrated haplogranitic melt ($\varphi_s = 0.00$) behaves as a Newtonian fluid at the imposed strain rates with a dynamic viscosity of $10^{10.3}$ Pa s at 500°C, in agreement with previous work on a similar silicic composition [Schulze et al., 1996; Dingwell et al., 1996]. Deformation remains homogeneous up to large strains ($\gamma = 8$), as evidenced both by the overall shape of the sample after the experiment (Figure 3) and by homogeneous deformation of the residual bubbles in the melt acting as perfect strain markers. For $\varphi_s = 0.16$, the shape preferred orientations of the bubble population yield an average orientation α that deviates significantly from the theoretical behavior known for ideally deformable (passive) markers submitted to bulk simple shear flow. This apparent discrepancy expresses a change in the general flow of the liquid (the matrix) that wraps around the suspended (solid) particles formed by alumina grains (Figure 15). This phenomenon is well documented in analogue simple shear experiments conducted on solid fractions as low as $\varphi_s = 0.1$ [Ildefonse et al., 1992]. In the case of an isolated rigid particle having a coherent interface with the surrounding fluid submitted to slow laminar flow, the streamlines deviate around the solid particle and form an asymmetric strain pattern. The maximum width of the perturbation in the fluid lies in the shear plane passing through the center of inertia of the particle, and depends on the viscosity of the fluid and, for a non-Newtonian matrix, on the flow rate [Ildefonse et al., 1992]. This heterogeneous strain pattern is well known in fluid mechanics for spherical bodies and has been extensively explored for anisometric particles in experimental studies on analogue materials [Ildefonse et al., 1992; Arbaret et al., 2001; Piazolo et al., 2002] and in numerical simulations (see Marques et al. [2005] for a recent review). All agree that the extension of the perturbed field in the direction of shear is about two times the maximum length of the rigid particle. Field examples are common in highly sheared ductile rocks where the geometry of the perturbed flow is often “fossilized” by both alignment of anisometric minerals and/or deformation of the soft polycrystalline groundmass around rotating “winged” porphyroclasts [Hanmer and Passchier, 1991]. Similar features are also typical in highly volcanic rocks with the alignment of microlites wrapping around phenocrysts and forming asymmetric tails [Smith, 2002]. For very low solid fractions ($\varphi_s \ll 0.1$), the distance between ideally distributed particles is theoretically enough to avoid any interaction between the flow perturbations caused by individual particles. For $\varphi_s > 0.1$, the distance between solid particles is statistically shorter (undeformed suspension HPG5 in Figures 1 and 8) and asymmetric strain patterns developed around particles coalesce (see also Arbaret et al. [1996, Figure 6] for illustration). Consequently, as recorded by residual bubbles in our experiments for $\varphi_s = 0.16$, the bulk direction of the streamlines makes an angle with the bulk shear direction that remains constant at large strains.

Measured shape fabrics of the solid fraction are characterized by a unimodal orientation α almost stable and parallel to the shear direction, and by an intensity R that decreases gradually with strain. As already pointed out in the introduction, such fabric development with strain is usually related to the combination of a heterogeneous distribution of particle aspect ratios and numerous transient interactions (i.e., collisions) between particles that occur because of the relative motion of the rigid particles in the sheared matrix [Blumenfeld and Bouchez, 1988; Tikoff and Teyssier, 1994; Philpotts and Asher, 1994; Arbaret et al., 1996; Stickel and Powell, 2005]. The proportion of interacting particles is difficult to quantify in two-dimensional sections. Two-dimensional analogue experiments on suspensions with similar solid fractions deformed by simple shear [Arbaret et al., 1996] have shown that, for shear strains larger than $\gamma \sim 5$, 50% of the particles are statistically involved in collisions.

4.4. Transition to Nonlinear Rheology ($\varphi_s = 0.34$)

For $\varphi_s = 0.34$ (PO609), the apparent viscosity of the magmatic suspension increases with crystal fraction and deformation progressively becomes nonlinear ($n > 1$) as the suspension evolves from a material containing isolated rotating porphyroclasts to one where interacting clasts result in complex structures and textures (Figure 15). These trains of imbricate particles whose long axis orientations control the orientation $\alpha \sim -7°$ of the whole SPO are more stable than tiling systems recognized in dilute suspensions and can survive and develop at large strains [Ildefonse et al., 1992; Tikoff and Teyssier, 1994]. In our experiments, the rare trains of particles that are present are mostly oriented at ~20° from the shear direction X (dark grey arrows in Figure 10). Similar orientations with respect to the bulk mineral foliation were evidenced for trains of feldspar megacrysts in the deformed Mono Creek Granite (Sierra Nevada, California) and assimilated to S/C fabrics [Tikoff and Teyssier, 1994; Berthé et al., 1979]. The development of such long rigid clusters induces a strong increase in tortuosity of the fluid as it is forced to wrap around them and flow along melt enriched channels bordered by parallel trains (Figure 15). This is well evidenced by isolated particles statistically oriented parallel to the elongation of these channels. Discrete melt-enriched zones similarly oriented with respect to the average orientation of grains in bordering aggregates are documented in lavas with basalt to dacite compositions [e.g., Smith, 1997] where such microstructures are possibly the cause of a deviation from Newtonian rheology.

[41] Complex flux line trajectories in the fluid and the formation of a crystal network may result in the onset of a finite yield strength τ_c [Petford and Koenders, 2001; Saar et al., 2001], although we have not been able to observe τ_c in our experiments. Studies based on percolation theory show that the value of the critical (crystal) volume fraction φ_c for the onset of crystal or particle network formation depends on particle shape and size distributions and on the particles' overall orientation distribution [Pike and Seager, 1974; Garboczi et al., 1995; Lorenz and Ziff, 2001; Saar et al., 2001]. For spheres φ_c is 0.2896 [Shante and Kirkpatrick, 1971; Lorenz and Ziff, 2001], a value approached for parallel-aligned convex object populations [Saar et al., 2001]. A minimum of $\varphi_c = 0.08$ is reached for randomly oriented and strongly flattened prisms [Saar et al., 2001; Saar and Manga, 2002]. In our starting microstructures, the crystal population is randomly oriented and characterized by an axial ratio of $R = 2.35 \pm 1.14$. On the basis of the assumption that the particles can be approximated as biaxial ellipsoids despite their heterogeneous size and shape, three-dimensional numerical models yield a percolation threshold $\varphi_c < \sim 0.25$ [Garboczi et al., 1995; Saar and Manga, 2002]. At large shear strains, a bulk shape preferred orientation is evidenced but remains weak, implying only a limited decrease in percolation threshold due to particle alignment. Accurate estimation of φ_c in these sheared suspensions remains difficult as it requires quantification in three dimensions of the anisotropic distribution of the solid phase and the possible formation of clusters and trains of particles.

4.5. Pseudoplastic and Cataclastic Fields ($\varphi_s \geq 0.54$)

At high solid fractions, magmatic suspensions have a pseudoplastic behavior that is thought to be controlled by a bridging solid crystal framework composed of both stable long trains and large clusters of particles [Pinkerton and Stevenson, 1992; Saar et al., 2001; Saar and Manga, 2002]. At $\varphi_s = 0.54$, the crystal network appears almost entirely connected in [XZ] sections. At large strains ($\gamma > 9.5$), the bulk shape fabric is organized into alternating orientation domains characterized by conjugate mineral orientations with respect to the direction of shear (white arrows and black arrows for PO516 and PO528 in Figure 12). These crystal alignment

domains are structures commonly found in crystal-rich lava flows deformed at large strain rates in dykes (trachyte dyke, Fraser Island [Smith, 2002]) and domes (Hradiště trachyte dome [Jančušková et al., 1992]) (Figure 15). Such structures are often associated with dilatancy [Smith, 1997]. Dilatancy is also characteristic of crystallizing mush at the base of granitic magmas emplaced at lower strain rates than lavas flows (10^{-10} s^{-1} [Petford, 2003]) and has been evidenced in quartz undergoing granular flow [Schmocker et al., 2003] and in quartz analogue (norcamphor) experiments [Bauer et al., 2000].

[43] Discrete local shear zones surrounded by aligned crystals and oriented at about 20°–30° with respect to the shear direction crosscut all alternating domains (PO516, Figure 12). They resemble shear bands marked by local alignment of crystals observed in highly viscous lavas such as trachyte [Nicolas, 1992], dacite [Smith, 1997] and phonolite domes [Arbaret et al., 1993]. These shear bands are usually interpreted as C' bands by analogy with the S/C associations developed in low to medium grade metamorphic rocks deformed to large strains [Berthé et al., 1979; Nicolas, 1992]. Similarly oriented melt-rich shear bands with synthetic normal sense of shear have been evidenced in partially molten rocks ($\varphi_s > 0.88$) experimentally deformed in a bulk simple shear regime [Rosenberg and Handy, 2000; Holtzman et al., 2003; Katz et al., 2006].

[44] At low temperatures (T = 500°C, PO524), a generalized cataclastic texture develops because of high local stresses at contact points between touching grains. It is formed by abundant fragments of dislocated grains, only a small number of grains having preserved their original size. This texture is characterized by a bulk extensional fabric parallel to the shortening direction (Figures 12 and 14a). Shear zones oriented at −30° from the shear direction are marked by well-dispersed fragments of dislocated grains that document the matrix deformation around preserved rotating grains and are consistent with a dextral sense of shear (Figure 14d). In other regions the original shape of dislocated grains is mostly preserved (Figure 14a). The organization of fragments and radial orientations of fractures indicates that the fragmentation started and propagated from the contact region between grains (Figure 14c). Similar brittle behavior commonly develops between touching phenocrysts [Smith, 2002] and is often observed at the base of lava flows and near conduit walls where it is interpreted as a consequence of intense, localized shear [Smith, 1996; Miura, 1999; Polacci et al., 2005]. Evidence of intragranular fracturing by contact interaction between particles is also visible in PO528 while it is only a minor process in PO516, an experiment where most of the deformation occurred at higher temperatures. These microstructures suggest that intragranular fracturing becomes more widespread with decreasing temperature, i.e., with increasing viscosity of the suspension. Complementary experiments exploring a larger strain rate range are needed to quantify the effect of deformation rate on the development of the observed cataclasites.

[45] At very high crystal fractions, evidence of strongly fragmented grains suggests intragranular fracturing due to high local stresses at contact points between grains (as in PO524, $\varphi_s = 0.54$; Figures 14a and 14c). However, a large number of broken grains show different fracturing patterns, with the presence of fractures parallel to the maximum principal stress. Regular spacing and parallelism of the fractures result in the breakup of grains into regularly shaped, almost parallelepipedic, fragments with an average shape preferred orientation that controls the bulk shape fabric of $\alpha \approx 68°$ measured over the section. Such morphology corresponds to the asymmetric domino boudin geometry commonly found in large strain shear zones developed in ductile high-grade terrains [Goscombe and Passchier, 2003] and in some volcanic rocks such as pyroxene fragments in a dacite (Katsurajima, Japan

[Smith, 2002]). Since PO612 ($\varphi_s = 0.65$) and PO516 ($\varphi_s = 0.54$) were deformed under similar experimental conditions (stepping experiments, Table 1) and to similar finite strains, the fracture mechanism may be due to the difference in crystal fraction in the two samples.

5. Conclusion

We carried out torsion experiments on synthetic magmatic suspensions composed of a water-undersaturated aluminosilicate melt with 2.5 wt % H_2O and various solid fractions of crushed alumina grains ($0.00 < \varphi_s < 0.76$). The chosen composition and experimental conditions (subsolidus temperatures of 475°C to 600°C and strain rates from 2.00×10^{-5} to 2.09×10^{-3} s^{-1}) are particularly relevant for silicic magmas either emplaced at shallow depths in subvolcanic dykes and sills or erupting at the surface to form domes and lava flows.

Pure hydrated haplogranitic melt ($\varphi_s = 0.00$) behaves like a Newtonian fluid at the imposed strain rates with a viscosity of $10^{10.3}$ Pa s at 500°C. Homogeneous deformation is recorded during the experiment by residual bubbles acting as perfect strain markers. From low to intermediate solid concentrations ($0.16 < \varphi_s < 0.54$), the shape fabrics of the solid fraction, measured on [XZ] sections, are characterized by a unimodal orientation that is almost stable and nearly parallel to the shear direction, and by an intensity that decreases gradually with strain. At fixed experimental conditions, the apparent viscosity increases with solid fraction, while the rheology becomes progressively pseudoplastic and can be modeled by a power law ($n > 1$). Both the shape fabric development and the change in rheological behavior originate from the increase in the number of particle clusters. Because the experiments were performed at high stresses, the possible onset of a finite yield strength could not be observed.

At high solid concentrations ($\varphi_s > 0.54$), the crystal network appears almost entirely connected in [XZ] sections. At $T \geq 550$°C, the bulk shape fabric of the solid fraction is organized into alternating orientation domains that are conjugate with respect to the direction of shear and that are crosscut by melt-enriched discrete shear zones surrounded by aligned crystals. At $T \leq 550$°C, intragranular fracturing of the alumina grains results from high local stresses at contact points between neighboring particles. The resulting bulk extensional fabric is almost parallel to the shortening direction and is crosscut by synthetic normal shear zones.

For $\varphi_s = 0.65$, the alumina grains form a fully interconnected solid framework and consequently undergo intense fracturing. Cataclastic processes include intragranular fracturing due to high local stresses at contact points between grains and the development of tensile fractures that form asymmetric structures resembling domino boudins. These structures control the orientation of the bulk shape fabric at about 68° from the shear direction and are associated with a shear thinning rheology.

Although magma composition, temperature and strain rate may be different in nature, results obtained in this study provide a framework for interpreting observed structures in terms of rheological evolution of magma flow during ascent and emplacement. The change in rheology from fast viscous flow to power law rheology due to degassing-induced crystallization is recognized to control the mode of ascent and surface emplacement of crystal-rich lavas, as highlighted by the observation of dome growth on active andesitic volcanoes such as the Merapi and Mount Unzen volcanoes or by the present-day eruption of the Soufrière hills volcano [e.g., Watts et al., 2002]. In this environment, the development of localization microstructures such as melt-filled shear bands and intragranular fracturing may play a key

role in the generation and persistence of ductile to brittle shear faults along sidewalls of magma conduits or on the surface of near-solid spines developed during the effusive phases of eruptions.

Notation

- A preexponential term ($MPa^{-n}\ s^{-1}$).
- a long axis of object (bubble or crystal) (μm).
- b short axis of object (bubble or crystal) (μm).
- Ca capillary number (dimensionless).
- d mean equivalent diameter of deformed bubbles (μm).
- n stress exponent (dimensionless).
- n_i number of analyzed subimages (dimensionless).
- n_o number of analyzed objects (bubbles or crystals) in image (dimensionless).
- l undeformed bubble radius (μm).
- Q activation energy for creep ($kJ\ mol^{-1}$).
- r axial ratio of object (bubble or crystal) (dimensionless).
- R measured axial ratio of shape fabric ellipse = SPO intensity (dimensionless).
- R_{th} theoretical axial ratio of shape fabric ellipse (dimensionless).
- T temperature (°C).
- T_g brittle-ductile transition temperature (°C).
- η melt viscosity (Pa s).
- η_{ap} apparent viscosity (Pa s).
- Φ_b bubble fraction (dimensionless).
- κ surface tension ($J\ m^{-2}$).
- Φ_c critical crystal volume fraction (dimensionless).
- Φ_s solid fraction (dimensionless).
- Ø diameter of crushed alumina crystals (μm).
- α orientation of long axis of shape fabric ellipse (degree).
- α_{th} theoretical orientation of long axis of shape fabric ellipse (degree).
- $\dot{\gamma}$ strain rate (s^{-1}).
- γ theoretical finite shear strain or total finite strain measured at maximum sample radius (dimensionless)
- γ_{sec} finite strain reached at the depth of the section of observation (dimensionless).
- γ_i incremental strain during stepping experiment (dimensionless).
- τ_c finite yield strength (Pa).

Acknowledgments

We wish to thank Jean-Pierre Burg for his continuous support and Renée Heilbronner and Patrick Launeau for useful discussions. L.A. and R.C. acknowledge support by the French Ministry of Education and Research (ACI JC3013, “Fabriques magmatiques”) and a Ph.D. fellowship for R.C. M.B. acknowledges support by the Swiss National Science Foundation (2000-0666.16 and 2-77410-04) in Zurich and by the European Social Fund in Toulouse. We also thank George Bergantz, Richard Katz, and Martin O. Saar for their comments and careful reviews of the manuscript.

References

Arbaret, L., and J.-P. Burg (2003), Complex flow in lowest crustal, anastomosing mylonites: Strain gradient in a Kohistan gabbro, northern Pakistan, J. Geophys. Res., 108(B10), 2467, doi:10.1029/2002JB002295.

Arbaret, L., H. Diot, and P. Launeau (1993), The phonolitic body of Petit Gerbier (eastern Velay, French Massif Central, France)—Magnetic and magmatic structures, C. R. Acad. Sci., Ser. II, 316, 1603–1610.

Arbaret, L., H. Diot, and J. L. Bouchez (1996), Shape fabrics of particles in low concentration suspensions: 2D analogue experiments and application to tiling in magma, J. Struct. Geol., 18, 941–950.

Arbaret, L., H. Diot, J. L. Bouchez, M. Blanquat, and P. Lespinasse (1997), Analogue 3D simple shear experiments of magmatic biotite subfabric, in Granites: From Segregation of Melt to Emplacement Fabrics, edited by J. L. Bouchez, D. H. W. Hutton, and W. E. Stephens, pp. 129–143, Kluwer Acad., Dordrecht, Netherlands.

Arbaret, L., N. S. Mancktelow, and J.-P. Burg (2001), Effect of shape and orientation on rigid particle rotation and matrix deformation in simple shear flow, J. Struct. Geol., 23, 113–125.

Arzi, A. (1978), Critical phenomena in the rheology of partially melted rocks, Tectonophysics, 44, 173–184.

Bagdassarov, N., and H. Pinkerton (2004), Transient phenomena in vesicular lava flows based on laboratory experiments with analogue materials, J. Volcanol. Geotherm. Res., 132, 115–136.

Bagdassarov, N. S., D. B. Dingwell, and S. L. Webb (1994), Viscoelasticity of crystal- and bubble-bearing rhyolite melt, Phys. Earth Planet. Inter., 83, 83–99.

Bagdassarov, N., A. Dorfman, and D. B. Dingwell (2000), Effect of alkalis, phosphorus, and water on the surface tension of haplogranite melt, Am. Mineral., 85, 33–40.

Barnhoorn, A., M. Bystricky, K. Kunze, L. Burlini, and J.-P. Burg (2005), Strain localization in bimineralic rocks: Experimental deformation of synthetic calcite-anhydrite aggregates, Earth Planet. Sci. Lett., 240, 748–763.

Bauer, P., S. Palm, and M. R. Handy (2000), Strain localization and fluid pathways in mylonite: Inferences from in situ deformation of a water-bearing quartz analogue (norcamphor), Tectonophysics, 320, 141–165.

Berthé, D., P. Choukroune, and P. Jagouzo (1979), Orthogneiss, mylonite and non-coaxial deformation of granites: The example of the South American shear zone, J. Struct. Geol., 1, 31–42.

Bindeman, I. N. (2005), Fragmentation phenomena in populations of magmatic crystals, Am. Mineral., 90, 1801–1815.

Blumenfeld, P., and J. L. Bouchez (1988), Shear criteria in granite and migmatite deformed in the magmatic and solid states, J. Struct. Geol., 10, 361–372.

Bouchez, J. L., D. H. W. Hutton, and W. E. Stephens (Eds.) (1997), Granites: From Segregation of Melt to Emplacement Fabrics, 358 pp., Kluwer Acad., Dordrecht, Netherlands.

Bystricky, M., K. Kunze, L. Burlini, and J.-P. Burg (2000), High shear strain of olivine aggregates: Rheological and seismic consequences, Science, 290, 1564–1567.

Bystricky, M., F. Heidelbach, and S. Mackwell (2006), Large-strain deformation and strain partitioning in polyphase rocks: Dislocation creep of olivine-magnesiowüstite aggregates, Tectonophysics, 427, 115–132.

Casey, M., K. Kunze, and D. L. Olgaard (1998), Texture of Solnhofen limestone deformed to high strains in torsion, J. Struct. Geol., 20, 255–267.

Chadwick, W. W., R. J. Archuleta, and D. A. Swanson (1988), The mechanics of ground deformation precursory to dome-building extrusions at Mount St. Helens 1981–1982, J. Geophys. Res., 93, 4351–4366.

Champallier, R. (2005), Déformation expérimentale à haute température et haute pression de magmas partiellement cristallisés, Ph.D. thesis, 191 pp., Univ. d'Orléans, Orleans, France.

Champallier, R., M. Bystricky, and L. Arbaret (2007), Experimental investigation of magma rheology at 300 MPa: From pure hydrous melt to 75 vol. % of crystals, Earth Planet. Sci. Lett., in press.

Costa, A. (2005), Viscosity of high crystal content melts: Dependence on solid fraction, Geophys. Res. Lett., 32, L22308, doi:10.1029/2005GL024303.

Daines, M. J., and D. L. Kohlstedt (1997), Influence of deformation on melt topology in peridotites, J. Geophys. Res., 102, 10,257–10,271.

Dell'Angelo, L., and J. Tullis (1988), Experimental deformation of partially melted granitic aggregates, J. Metamorph. Geol., 6, 495–515.

Dingwell, D. B. (1997), The brittle-ductile transition in high-level granitic magmas: Material constraints, J. Petrol., 38, 1635–1644.

Dingwell, D. B. (1998), The glass transition in hydrous granitic melts, Phys. Earth Planet. Inter., 107, 1–8.

Dingwell, D. B., N. S. Bagdassarov, G. Y. Bussod, and S. L. Webb (1993), Magma rheology, in Experiments at High Pressure and Applications to the Earth's Mantle, Short Course Handbk., vol. 21, edited by R. W. Luth, pp. 131–196, Mineral. Assoc. of Can., Quebec, Que., Canada.

Dingwell, D. B., C. Romano, and K.-U. Hess (1996), The effect of water on the viscosity of a haplogranitic melt under P-T-X conditions relevant to silicic volcanism, Contrib. Mineral. Petrol., 124, 19–28.

Fernandez, A., and J. Fernandez-Catuxo (1997), 3D biotite shape fabric experiments under simple shear strain, in Granites: From Segregation of Melt to Emplacement Fabric, edited by J. L. Bouchez, D. H. W. Hutton, and W. E. Stephens, pp. 145–158, Kluwer Acad., Dordrecht, Netherlands.

Fernandez, A. N., and D. Gasquet (1994), Relative rheological evolution of chemically contrasted coeval magmas: Example of the Tichka plutonic complex (Morocco), Contrib. Mineral. Petrol., 116, 316–326.

Fernandez, A. N., J. L. Feybesse, and J. F. Mezure (1983), Theoretical and experimental study of fabrics developed by different shaped markers in two-dimensional simple shear, Bull. Soc. Geol. Fr., 25(3), 319–326.

Frost, H. J., and M. F. Ashby (1982), Deformation-Mechanism Maps: The Plasticity and Creep of Metals and Ceramics, 167 pp., Pergamon, New York.

Garboczi, E. J., K. A. Snyder, J. F. Douglas, and M. F. Thorpe (1995), Geometrical percolation threshold of overlapping ellipsoids, Phys. Rev. E, 52, 819–828.

Goscombe, B. D., and C. W. Passchier (2003), Asymmetric boudins as shear sense indicators—An assessment from field data, J. Struct. Geol., 25, 575–589.

Hanmer, S., and C. Passchier (1991), Shear-sense indicators: A review, Pap. 90-17, 72 pp., Geol. Surv. of Can., Ottawa, Ont., Canada.

Heidelbach, F., I. Stretton, F. Langenhorst, and S. Mackwell (2003), Fabric evolution during high shear strain deformation of magnesiowüstite ($Mg_{0.8}Fe_{0.2}O$), J. Geophys. Res., 108(B3), 2154, doi:10.1029/2001JB001632.

Hinch, E. G., and A. Acrivos (1980), Long slender drops in a simple shear flow, J. Fluids Mech., 90, 305–328.

Hirth, G., and D. L. Kohlstedt (1995a), Experimental constraints on the dynamics of the partially molten upper mantle: Deformation in the diffusion creep regime, J. Geophys. Res., 100, 1981–2001.

Hirth, G., and D. L. Kohlstedt (1995b), Experimental constraints on the dynamics of the partially molten upper mantle: 2. Deformation in the dislocation creep regime, J. Geophys. Res., 100, 15,441–15,449.

Holtz, F., M. Pichavant, P. Barbey, and W. Johannes (1992), Effects of H_2O on liquidus phase relations in the haplogranite system at 2 and 5 kbar, Am. Mineral., 77, 1223–1241.

Holtzman, B. K., D. L. Kohlstedt, M. E. Zimmerman, F. Heidelbach, T. Hiraga, and J. Hustoft (2003), Melt segregation and strain partitioning: Implications for seismic anisotropy and mantle flow, Science, 301, 1227–1230.

Holtzman, B. K., D. L. Kohlstedt, and J. P. Morgan (2005), Viscous energy dissipation and strain partitioning in partially molten rocks, J., 1–24, doi:10.1093/petrology/egi065.

Ildefonse, B., P. Launeau, J.-L. Bouchez, and A. Fernandez (1992), Effect of mechanical interactions on the development of shape preferred orientations: A two-dimensional approach, J. Struct. Geol., 14, 73–83.

Ildefonse, B., L. Arbaret, and H. Diot (1997), Rigid particles in simple shear flow: Is their preferred orientation periodic or steady state?, in Granites: From Segregation of Melt to Emplacement Fabrics, edited by J. L. Bouchez, D. H. W. Hutton, and W. E. Stephens, pp. 177–185, Kluwer Acad., Dordrecht, Netherlands.

Jančušková, Z., K. Schulmann, and R. Melka (1992), Relation entre fabriques de la sanidine et mise en place des magmas trachytiques (exemple du massif de Hradište, Bohême du nord), Geodin. Acta, 5, 235–244.

Jeffery, G. B. (1922), The motion of ellipsoidal particles immersed in a viscous fluid, Proc. R. Soc. London, Ser. A, 102, 161–179.

Ježek, J., R. Melka, K. Schulmann, and Z. Venera (1994), The behaviour of rigid triaxial particles in viscous flows: Modelling of fabric evolution in a multiparticle system, Tectonophysics, 229, 165–180.

Katz, R., M. Spiegelman, and B. Holtzman (2006), The dynamics of melt and shear localization in partially molten aggregates, Nature, 442(7103), 676–679.

Launeau, P. (2004), Mise en evidence des écoulement magmatiques par analyse d'image 2-D des distributions 3-D d'Orientations préférentielles de Formes, Bull. Soc. Geol. Fr., 175, 331–350.

Launeau, P., and A. R. Cruden (1998), Magmatic fabric acquisition mechanism in a syenite: Results of a combined anisotropy of magnetic susceptibility and image analysis method, J. Geophys. Res., 103, 5067–5089.

Launeau, P., and P.-Y. F. Robin (1996), Fabric analysis using the intercept method, Tectonophysics, 267, 91–119.

Launeau, P., J. L. Bouchez, and K. Benn (1990), Shape preferred orientation of object populations: Automatic analysis of digitized images, Tectonophysics, 180, 201–211.

Lejeune, A. M., and P. Richet (1995), Rheology of crystal-bearing silicate melts: An experimental study at high viscosities, J. Geophys. Res., 100, 4215–4229.

Lisle, R. J. (1985), Geological Strain Analysis, 99 pp., Pergamon, New York.

Llewellin, E. W., and M. Manga (2005), Bubble rheology and implication for conduit flow, J. Volcanol. Geotherm. Res., 143, 205–217.

Lofgren, G. (1980), Experimental studies on the dynamic crystallization of silicate melts, in Physics of Magmatic Processes, edited by R. B. Hargraves, pp. 488–550, Princeton Univ. Press, Princeton, N. J.

Lorenz, C. D., and R. M. Ziff (2001), Precise determination of the critical percolation threshold for the three-dimensional "Swiss cheese" model using a growth algorithm, J. Chem. Phys., 114, 3659–3661.

Manga, M., J. Castro, K. Cashman, and M. Loewenberg (1998), Rheology of bubble-bearing magmas, J. Volcanol. Geotherm. Res., 87, 15–28.

March, A. (1932), Mathematische Theorie der Regelung nach der Korngestalt bei affiner Deformation, Z. Kristallogr. Kristallgeom. Kristallphys., 81, 285–297.

Marques, F. O., R. Taborda, and J. Antunes (2005), Influence of a low-viscosity layer between rigid inclusion and viscous matrix on inclusion rotation and matrix flow: A numerical study, Tectonophysics, 407, 101–115.

Martel, C., D. B. Dingwell, O. Spieler, M. Pichavant, and M. Wilke (2001), Experimental fragmentation of crystal- and vesicle-bearing silicic melts, Bull. Volcanol., 63, 398–405.

Mecklenburgh, J., and E. H. Rutter (2003), On the rheology of partially molten synthetic granite, J. Struct. Geol., 25, 1575–1585.

Mecklenburgh, J., Y. H. Zhao, F. Heidelbach, and S. Mackwell (2006), Deformation of olivine-spinel aggregates in the system $(Mg,Ni)_2GeO_4$ deformed to high strain in torsion: Implications for upper mantle anisotropy, J. Geophys. Res., 111, B11209, doi:10.1029/2006JB004285.

Miura, D. (1999), Arcuate pyroclastic conduits, ring faults, and coherent floor at Kumano caldera, southwest Honshu, Japan, J. Volcanol. Geotherm. Res., 92, 271–294.

Murase, T., and A. R. McBirney (1973), Properties of some common igneous rocks and their melt at high temperature, Geol. Soc. Am. Bull., 84, 3563–3592.

Nicolas, A. (1992), Kinematics in magmatic rocks with special reference to gabbros, J. Petrol., 33, 891–915.

Paquet, J., and P. François (1980), Experimental deformation of partially melted granitic rocks at 600–900°C and 250 MPa confining pressure, Tectonophysics, 68, 131–146.

Paterson, M. S., and D. L. Olgaard (2000), Rock deformation tests to large shear strain in torsion, J. Struct. Geol., 22, 1341–1358.

Paterson, S. R., T. Fowler, K. L. Schmidt, A. S. Yoshinobu, E. S. Yuan, and R. B. Miller (1998), Interpreting magmatic fabrics patterns in plutons, Lithos, 44, 53–82.

Petford, N. (2003), Rheology of granitic magmas during ascent and emplacement, Annu. Rev. Earth Planet. Sci., 31, 399–427.

Petford, N., and M. A. Koenders (2001), Consolidation phenomena in sheared granitic magma: Effects of grain size and tortuosity, Phys. Chem. Earth, 26, 281–286.

Philpotts, A. R., and P. M. Asher (1994), Magmatic flow-direction indicators in a giant diabase feeder dike, Geology, 22, 363–366.

Piazolo, S., P. D. Bons, and C. W. Passchier (2002), The influence of matrix rheology and vorticity on fabric development of populations of rigid objects during plane strain deformation, Tectonophysics, 351, 315–329.

Pike, G. E., and C. H. Seager (1974), Percolation and conductivity: A computer study, Phys. Rev. B, 10, 1421–1433.

Pinkerton, H., and R. J. Stevenson (1992), Methods of determining the rheological properties of magmas at sub-liquidus temperatures, J. Volcanol. Geotherm. Res., 53, 47–66.

Poirier, J.-P. (1985), Creep of Crystals, 260 pp., Cambridge Univ. Press, Cambridge, U. K.

Polacci, M., M. Rosi, P. Landi, A. Di Muro, and P. Papale (2005), Novel interpretation for shift between eruptive styles in some volcanoes, Eos Trans. AGU, 87, 335–336.

Ramsay, J. G. (1967), Folding and Fracturing of Rocks, 568 pp., McGraw-Hill, New York.

Ramsay, J. G., and R. H. Graham (1970), Strain variation in shear belts, Can. J. Earth Sci., 7, 786–813.

Roscoe, R. (1952), The viscosity of suspensions of rigid spheres, Br. J. Appl. Phys., 3, 267–269.

Rosenberg, C. L., and M. R. Handy (2000), Syntectonic melt pathway during simple shearing of a partially molten rock analogue (norcamphor-benzamide), J. Geophys. Res., 105, 500–521.

Rosenberg, C. L., and M. R. Handy (2005), Experimental deformation of partially melted granite revisited: Implication for the continental crust, J. Metamorph. Geol., 23, 19–28.

Rutter, E. H., and D. H. K. Neumann (1995), Experimental deformation of partially molten Westerly granite under fluid-absent conditions, with implications for the extraction of granitic magmas, J. Geophys. Res., 100, 15,697–15,715.

Rybacki, E., M. S. Paterson, R. Wirth, and G. Dresen (2003), Rheology of calcite-quartz aggregates deformed to large strain in torsion, J. Geophys. Res., 108(B2), 2089, doi:10.1029/2002JB001833.

Saar, M. O., and M. Manga (2002), Continuum percolation for randomly oriented soft-core prism, Phys. Rev. E, 65, 056,131.

Saar, M. O., M. Manga, K. V. Cashman, and S. Fremouw (2001), Numerical models of the onset of yield strength in crystal-melt suspensions, Earth Planet. Sci. Lett., 187, 367–379.

Saltikov, S. A. (1958), Stereometric Metallography, 2nd ed., Metallurgizdat, Moscow.

Scaillet, B., F. Holtz, and M. Pichavant (1997), Rheological properties of granitic magmas in their crystallisation range, in Granite: From Segregation of Melt to Emplacement Fabrics, edited by J. L. Bouchez, D. Hutton and W. E. Stephen, pp. 11–29, Kluwer Acad., Dordrecht, Netherlands.

Scaillet, B., F. Holtz, A. Whittington, and M. Pichavant (1998), Phase equilibrium constraints on the viscosity of silicic magmas: 1. Volcanic-plutonic comparison, J. Geophys. Res., 103, 27,257–27,266.

Schmocker, M., M. Bystricky, K. Kunze, L. Burlini, H. Stünitz, and J.-P. Burg (2003), Granular flow and Riedel band formation in water-rich quartz aggregates experimentally deformed in torsion, J. Geophys. Res., 108(B5), 2242, doi:10.1029/2002JB001958.

Schulze, F., H. Behrens, F. Holtz, J. Roux, and W. Johannes (1996), The influence of H_2O on the viscosity of a haplogranitic melt, Am. Mineral., 81, 1155–1165.

Scott, T., and D. L. Kohlstedt (2006), The effect of large melt fraction on the deformation behavior of peridotite, Earth Planet. Sci Lett., 246, 177–187.

Shante, V. K. S., and S. Kirkpatrick (1971), An introduction to percolation theory, Adv. Phys., 20, 325–357.

Smith, J. V. (1996), Ductile-brittle transition structures in the basal shear zone of a rhyolite lava flow, eastern Australia, J. Volcanol. Geotherm. Res., 72, 217–223.

Smith, J. V. (1997), Shear thickening dilatancy in crystal-rich flows, J. Volcanol. Geotherm. Res., 79, 1–8.

Smith, J. V. (2002), Structural analysis of flow-related textures in lavas, Earth Sci. Rev., 57, 279–297.

Spera, J., A. Borgia, and J. Strimple (1988), Rheology of melts and magmatic suspensions: 1. Design and calibration of concentric cylinder viscometer with application to rhyolitic magma, J. Geophys. Res., 93, 10,273–10,294.

Stein, D. J., and J. Spera (1992), Rheology and microstructure of magmatic emulsions: Theory and experiments, J. Volcanol. Geotherm. Res., 49, 157–174.

Stein, D. J., and J. Spera (2002), Shear viscosity of rhyolite-vapor emulsions at magmatic temperatures by concentric cylinder rheometry, J. Volcanol. Geotherm. Res., 113, 243–258.

Stickel, J. J., and R. L. Powell (2005), Fluid mechanics and rheology of dense suspensions, Annu. Rev. Fluid Mech., 37, 129–149.

Tikoff, B., and C. Teyssier (1994), Strain and fabric analyses based on porphyroclast interaction, J. Struct. Geol., 16, 477–491.

van der Molen, I., and M. S. Paterson (1979), Experimental deformation of partially-melted granite, Contrib. Mineral. Petrol., 70, 299–318.

Vigneresse, J.-L., P. Barbey, and M. Cuney (1996), Rheological transitions during partial melting and crystallisation with application to felsic magma segregation and transfer, J. Petrol., 37, 1579–1600.

Watts, R. B., R. A. Herd, R. S. J. Sparks, and S. R. Young (2002), Growth patterns and emplacement of the andesitic lava dome at Soufrière Hills Volcano, Montserrat, in The Eruption of Soufrière Hills Volcano, Montserrat, From 1995 to 1999, edited by T. H. Druitt and B. P. Kokelaar, Mem. Geol. Soc. London, 21, 115–152.

Willis, D. G. (1977), A kinematic model of preferred orientation, Geol. Soc. Am. Bull., 88, 883–894.

Zimmerman, M. E., and D. L. Kohlstedt (2004), Rheological properties of partially molten lherzolite, J. Petrol., 45, 275–298.

Figures

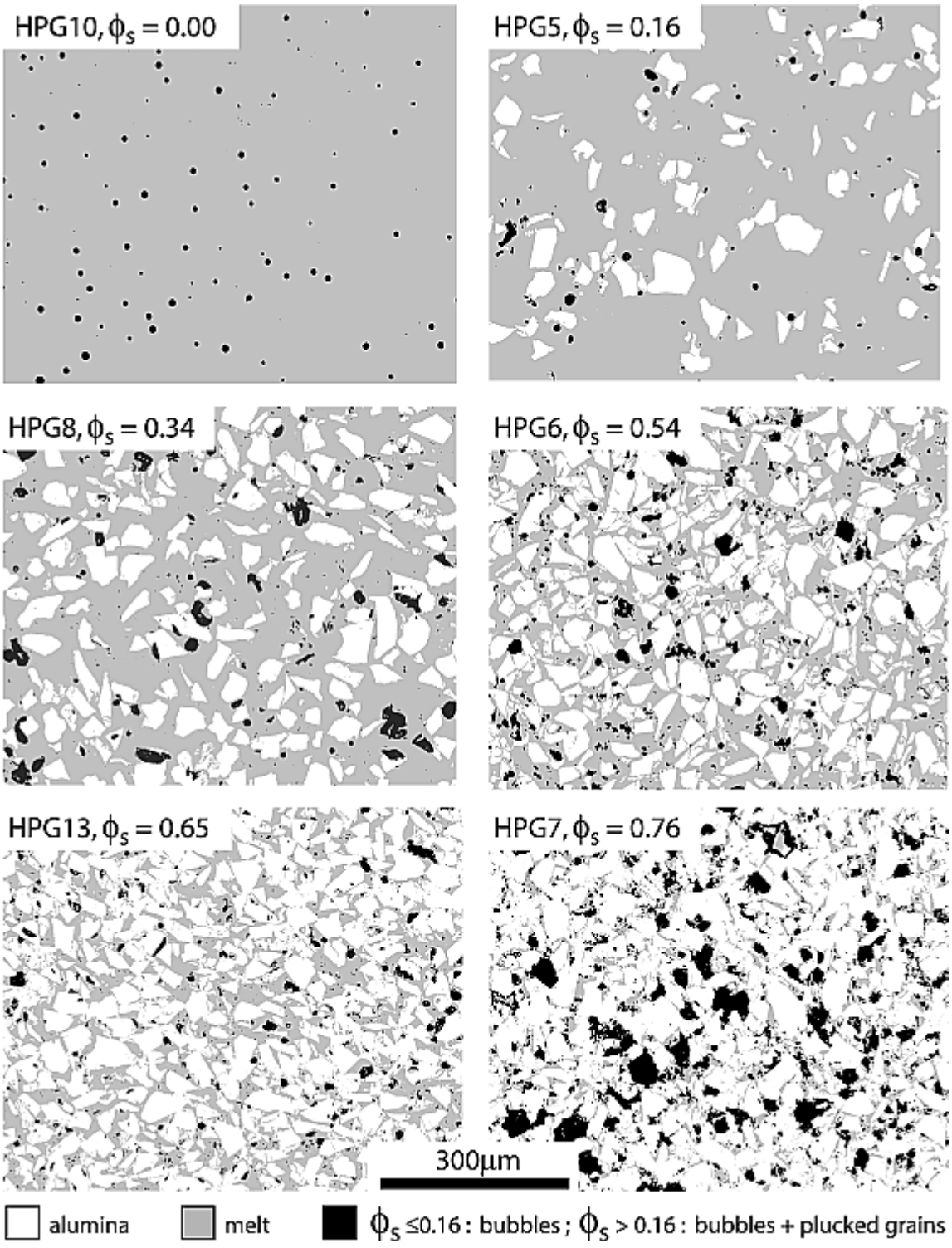

Figure 1. Segmented images of the starting materials with crystal fractions (φ_s) ranging from 0 to 0.76. Grey is interstitial melt, white areas are alumina grains, and black areas are residual bubbles (e.g., black circles, $\varphi_s = 0$ and 0.16) or regions where alumina grains were plucked during the polishing process (especially for $\varphi_s \geq 0.34$). Because the proportion of plucked grains increases with crystal fraction, individual residual bubbles are not distinguishable for $\varphi_s \geq 0.34$. Enhanced EPS

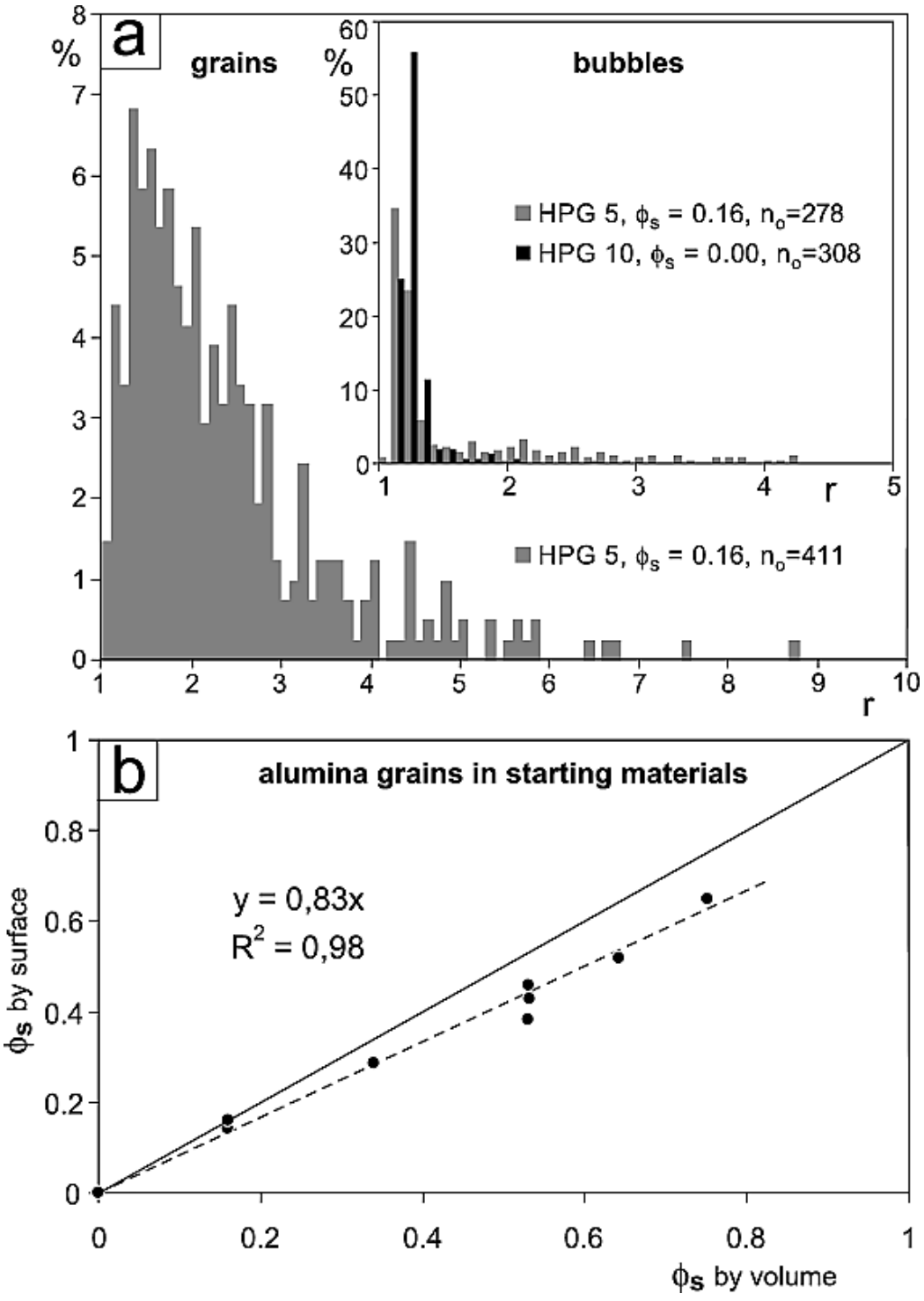

Figure 2. (a) Distribution of the aspect ratio r of bubbles and alumina grains in HPG5 (φ_s = 0.16). (inset) Comparison between the distributions of the aspect ratio of bubbles in HPG5 (φ_s = 0.16) and in crystal-free melt (HPG10, φ_s = 0.00). Here n_o is number of analyzed objects in each population. (b) Total surface area of alumina phase measured on polished [XZ] sections of the starting materials as a function of volume fraction used during sample synthesis. The regression line constrained to pass through the origin gives a slope of 0.83 (dashed line). Enhanced EPS

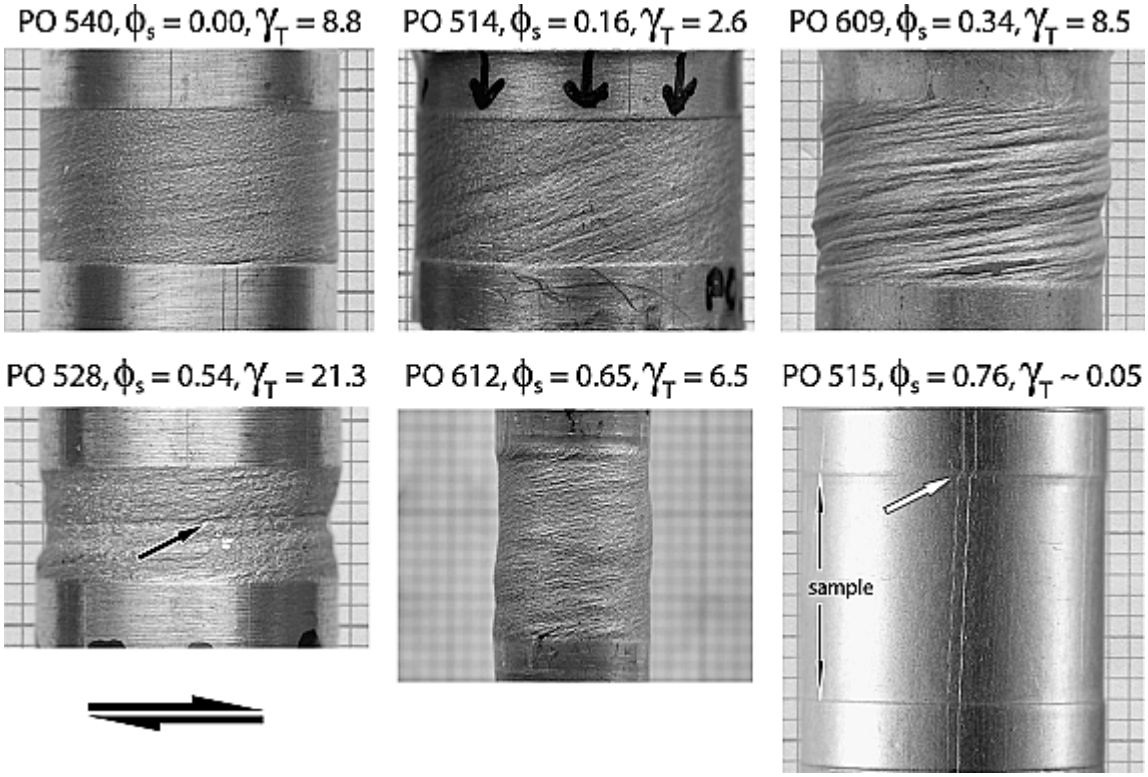

Figure 3. Photographs of deformed samples held between alumina pistons and still encapsulated in copper jackets. Sample positions are recognizable by the sheared jackets, with occasional deep grooves due to localization of deformation (particularly pronounced for PO609 and PO528, e.g., black arrow). Vertical lines that were scratched on the jackets before the experiments serve as deformation markers for samples deformed to low total strains. The inclination of two such parallel lines on sample PO515 indicates homogeneous shear deformation of $\gamma \sim 0.05$ before slip occurred at the interface between sample and top alumina spacer (offset shown by white arrow). Enhanced EPS

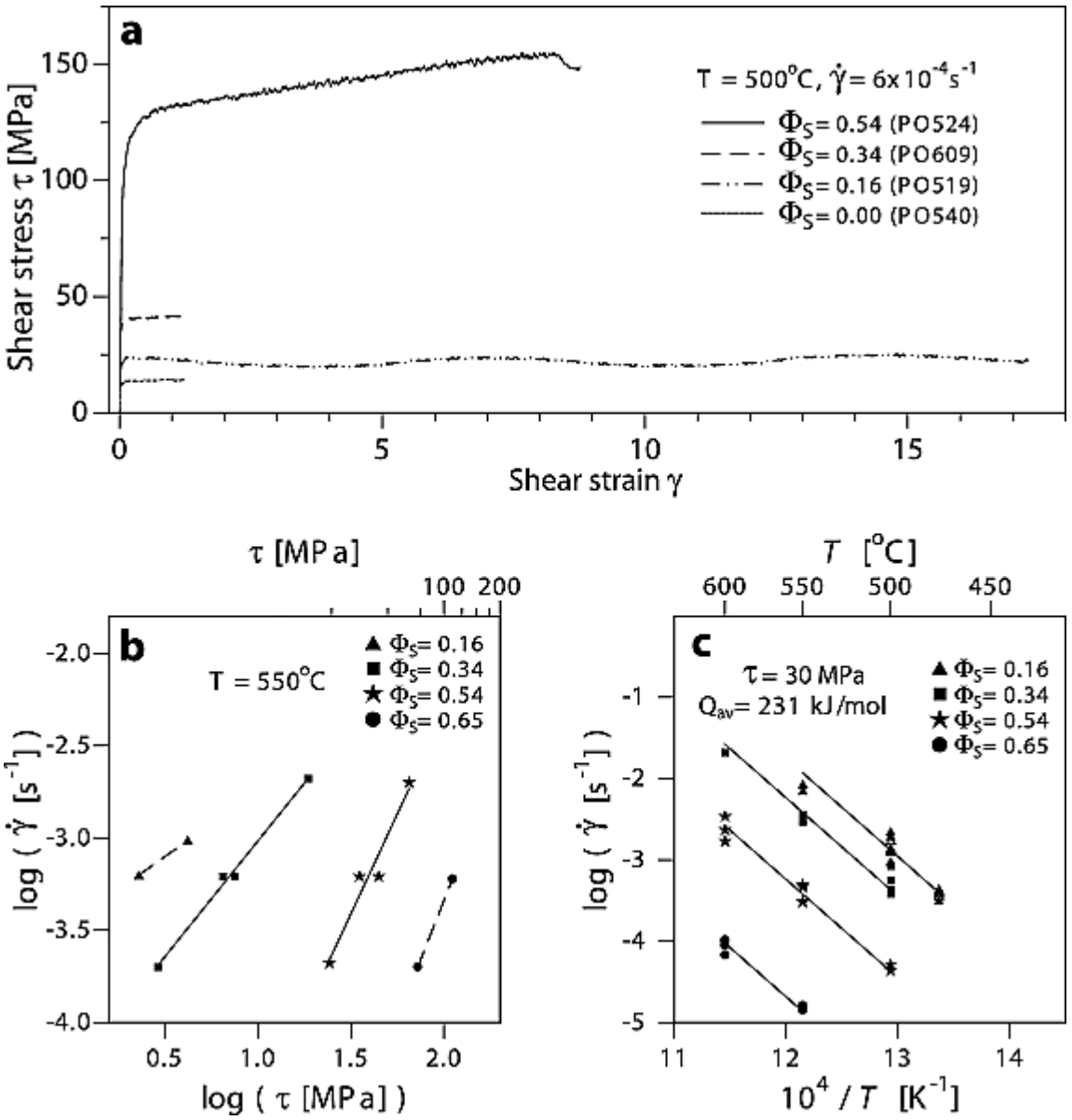

Figure 4. Selected mechanical data for magmatic suspensions with different solid fractions ($0.0 \leq \Phi_s \leq 0.65$). (a) Shear stress versus shear strain curves for samples deformed at a temperature T = 500°C and a shear strain rate $\dot{\gamma} \sim 6 \times 10^{-4}$ s^{-1}. (b) Shear strain rate versus shear stress data (steady state values or values after yield point) for samples deformed at T = 550°C. (c) Shear strain rate versus inverse temperature data after normalization to τ = 30 MPa using the stress exponent values listed in Table 2. Enhanced EPS

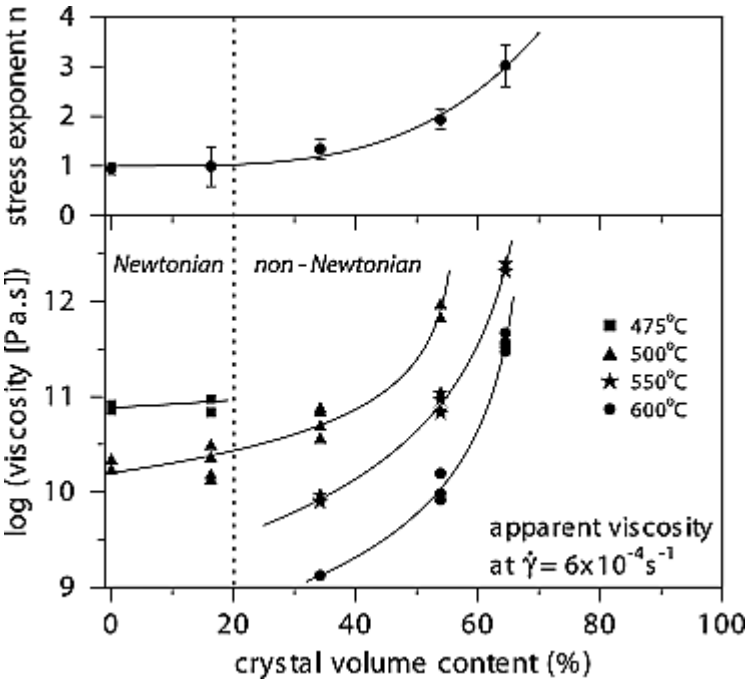

Figure 5. Variation of stress exponent (n) and apparent viscosity at $\dot{\gamma} = 6 \times 10^{-4}\ s^{-1}$ (η_{ap}) as a function of crystal fraction. For the apparent viscosity calculations all experimental data were normalized to $\dot{\gamma} = 6 \times 10^{-4}\ s^{-1}$ using the corresponding stress exponents. Enhanced EPS

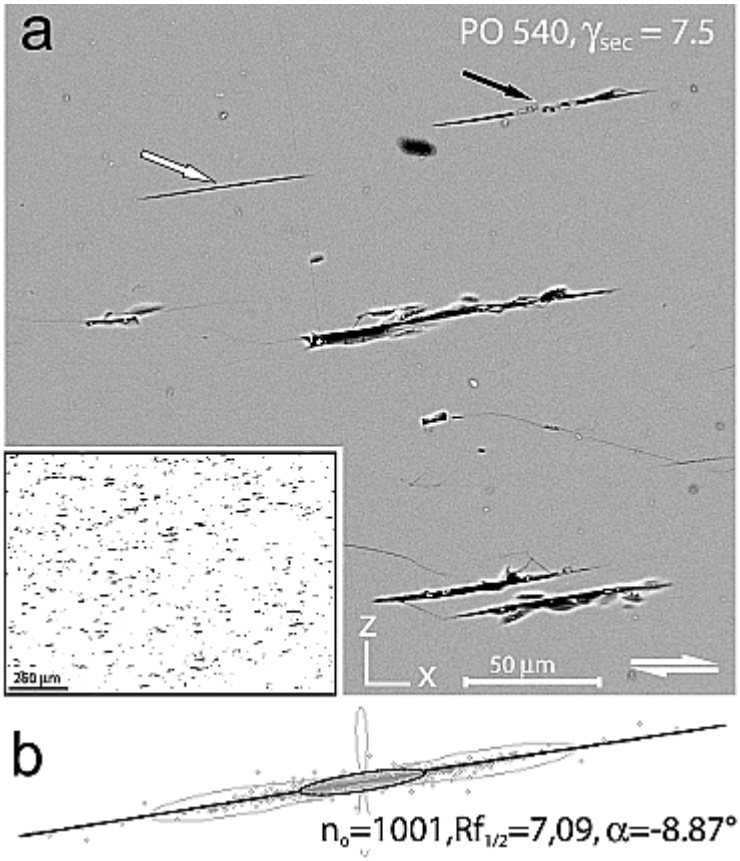

Figure 6. (a) Scanning electron microscope (SEM) image in [XZ] section of deformed crystal-free melt (PO540). The estimated finite shear strain of the analyzed section is γ_{sec} = 7.5. Black objects are residual bubbles and take up 0.9% of the total surface. Mean length of the bubbles' long axis is 9.9 ± 9.6 µm, with a maximum of 70.4 µm. White arrow points to a perfectly deformed bubble with a well-preserved shape. Black arrow points to an example of a bubble that has suffered both boudinage and fracturation. After segmentation of the image during analysis such an object is viewed as two identically oriented objects but with lower aspect ratios than the preserved bubble. Other bubbles on the image are affected by microcracks that have induced irregular borders during polishing. (inset) Full segmented image used for analysis. (b) Resulting Rf/Phi fabric ellipse obtained from analysis of n_o = 1001 bubbles. $Rf_{1/2}$ is the average axial ratio, and α is the orientation of the average long axis with respect to the direction of dextral shear (α < 0 when anticlockwise, sign convention shown in Figure 7). Bubbles with an average diameter of less that 2.4 µm, corresponding to less than 16 pixels at the resolution scale of the analyzed image, were not taken in consideration for the shape fabric calculation. Enhanced EPS

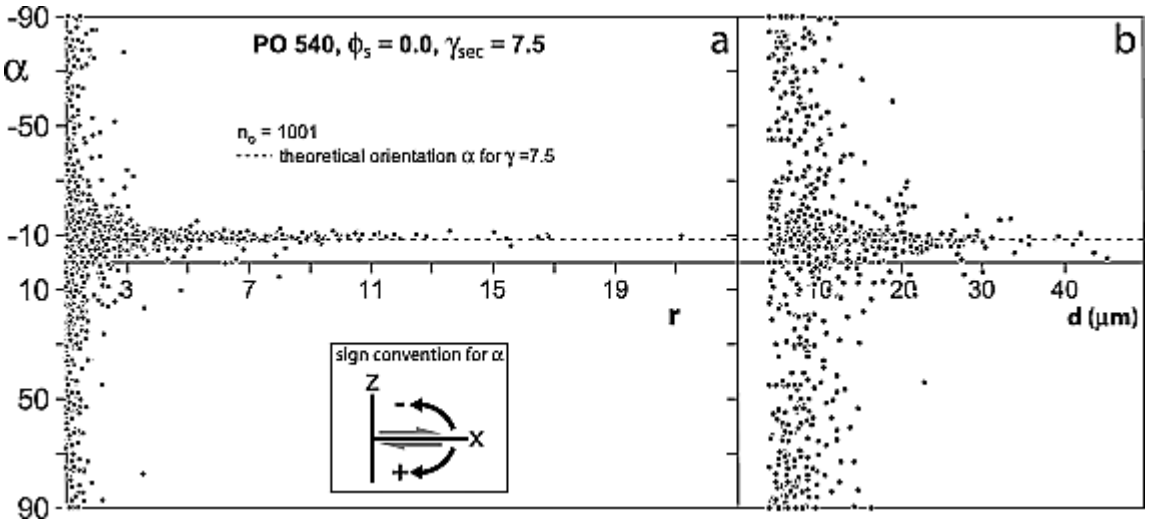

Figure 7. (a) Rf/Phi–like diagram giving the distribution of long axis orientations α versus aspect ratios r of residual bubbles measured in [XZ] section (γ_{sec} = 7.5) of deformed crystal-free melt (PO540). The horizontal dashed line corresponds to the orientation α of an ideal passive marker theoretically deformed to γ = 7.5. (inset) Sign convention used in this study for the long axis orientation α of analyzed objects and shape fabric ellipses of object populations. (b) Orientation α versus mean equivalent diameter d of residual bubbles. Here d corresponds to the diameter of an ideal isotropic disk having the same surface as the elongated bubbles measured in [XZ] sections. Enhanced EPS

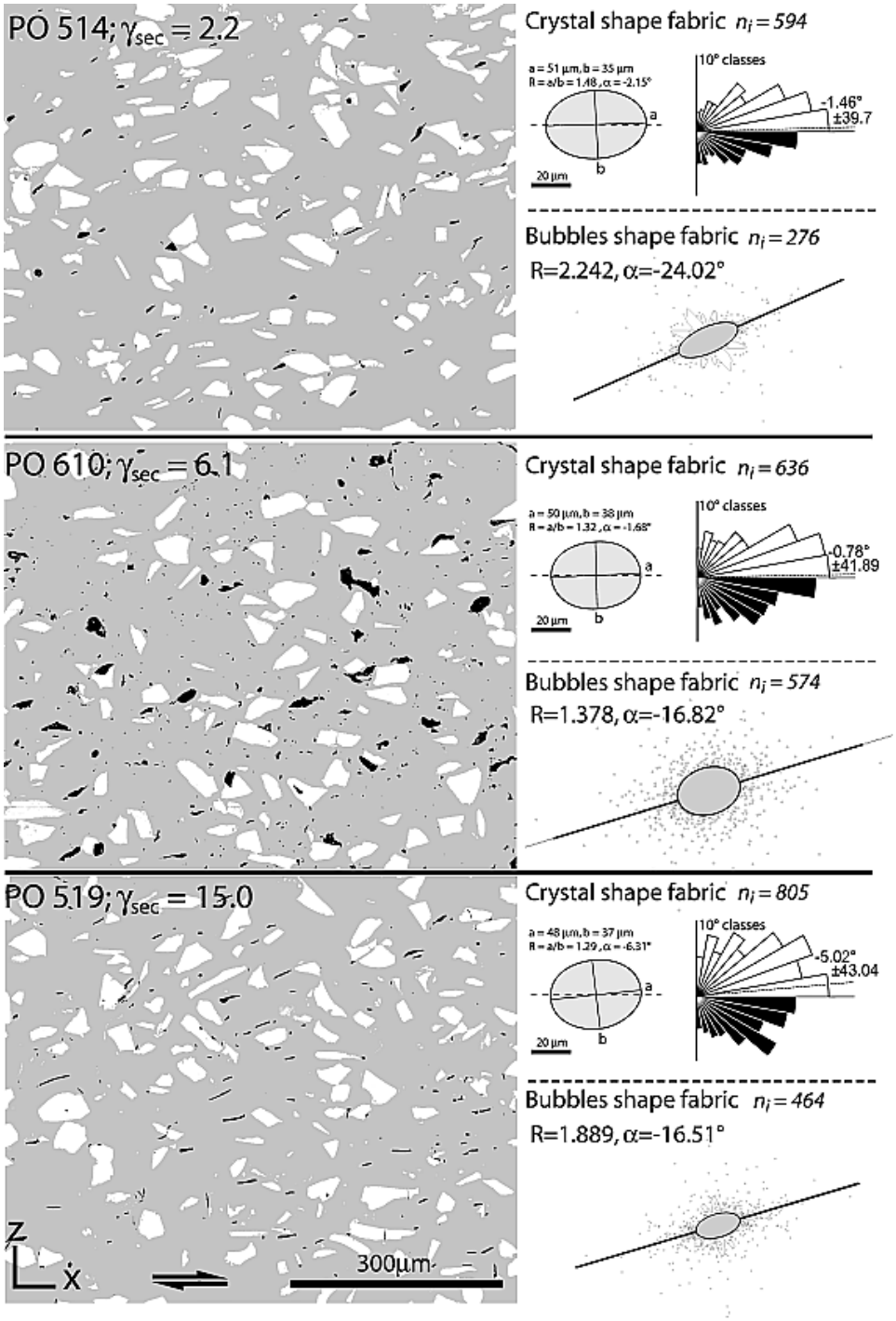

Figure 8. (left) False grey-level images of [XZ] sections of three samples with Ψ_s = 0.16 deformed to different finite shear strains. Here γ_{sec} are estimated finite shear strains of respective analyzed sections. Grey is interstitial melt, white areas are alumina grains, and black areas are residual bubbles or regions were grains were plucked during the polishing process (note extensive plucking in PO610). (right) For each sample, shape fabric of the alumina grain population expressed by the mean inertia tensor ellipse calculated from single object inertia tensors (orientations shown on rose diagram) and shape fabric of the residual bubble population determined by the Rf/Phi method. Enhanced EPS

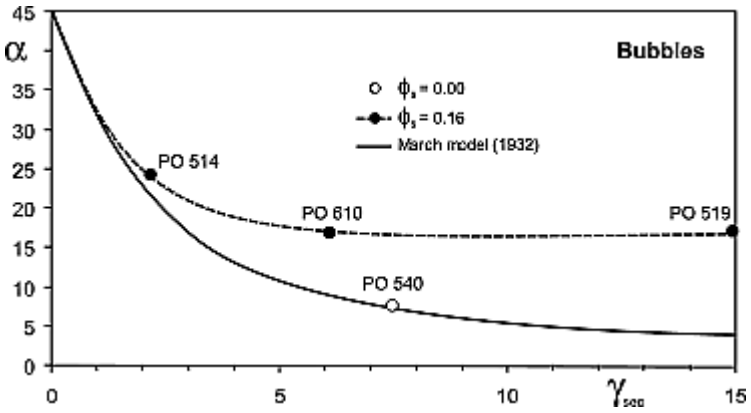

Figure 9. Orientation α (in degrees) of bubble fabrics versus finite strain γ_{sec} in analyzed sections. For $\varphi_s = 0.00$, α fits with the orientation of an ideal passive marker predicted by the March [1932] model (solid line), while for $\varphi_s = 0.16$, α deviates by about 15° from this model at large finite strains (dashed line). Enhanced EPS

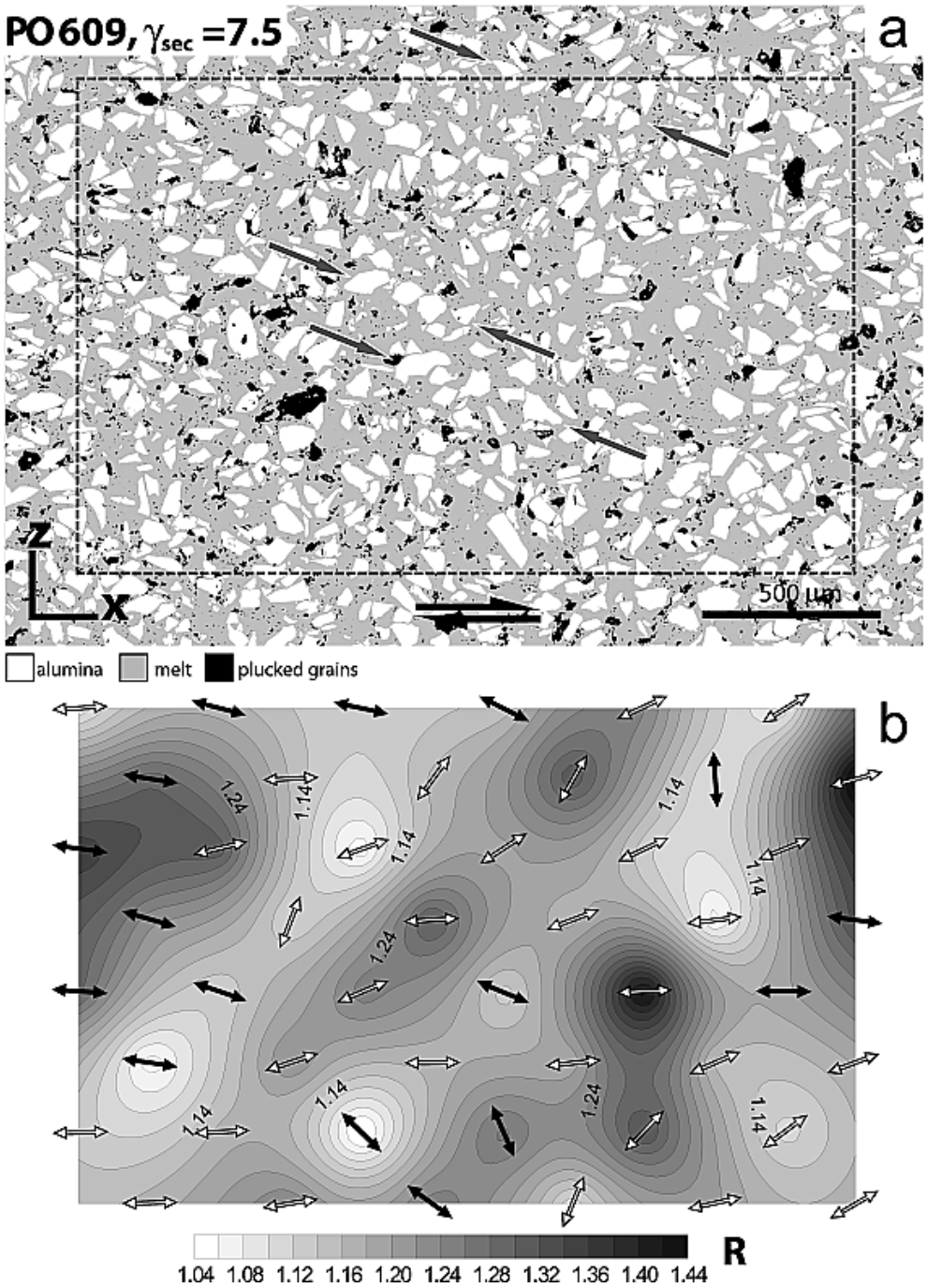

Figure 10. (a) False grey-level image of [XZ] section (γ_{sec} = 7.5) of PO609 (φ_s = 0.34). Dashed black square delimits the area used for R mapping. Dark grey arrows point out the orientation (~20°) and delimit the extent of trains of imbricate particles. (b) R map calculated by the kriging method. Local SPO directions α for alumina grains were determined in small areas within the image and are indicated by arrows. Numbers represent R values of corresponding contour lines. White arrows indicate "negative" orientations; black arrows indicate "positive" orientations (sign convention in Figure 7). Calculations were done using the intercept method with an angular counting step of 9° in a circular window. Enhanced EPS

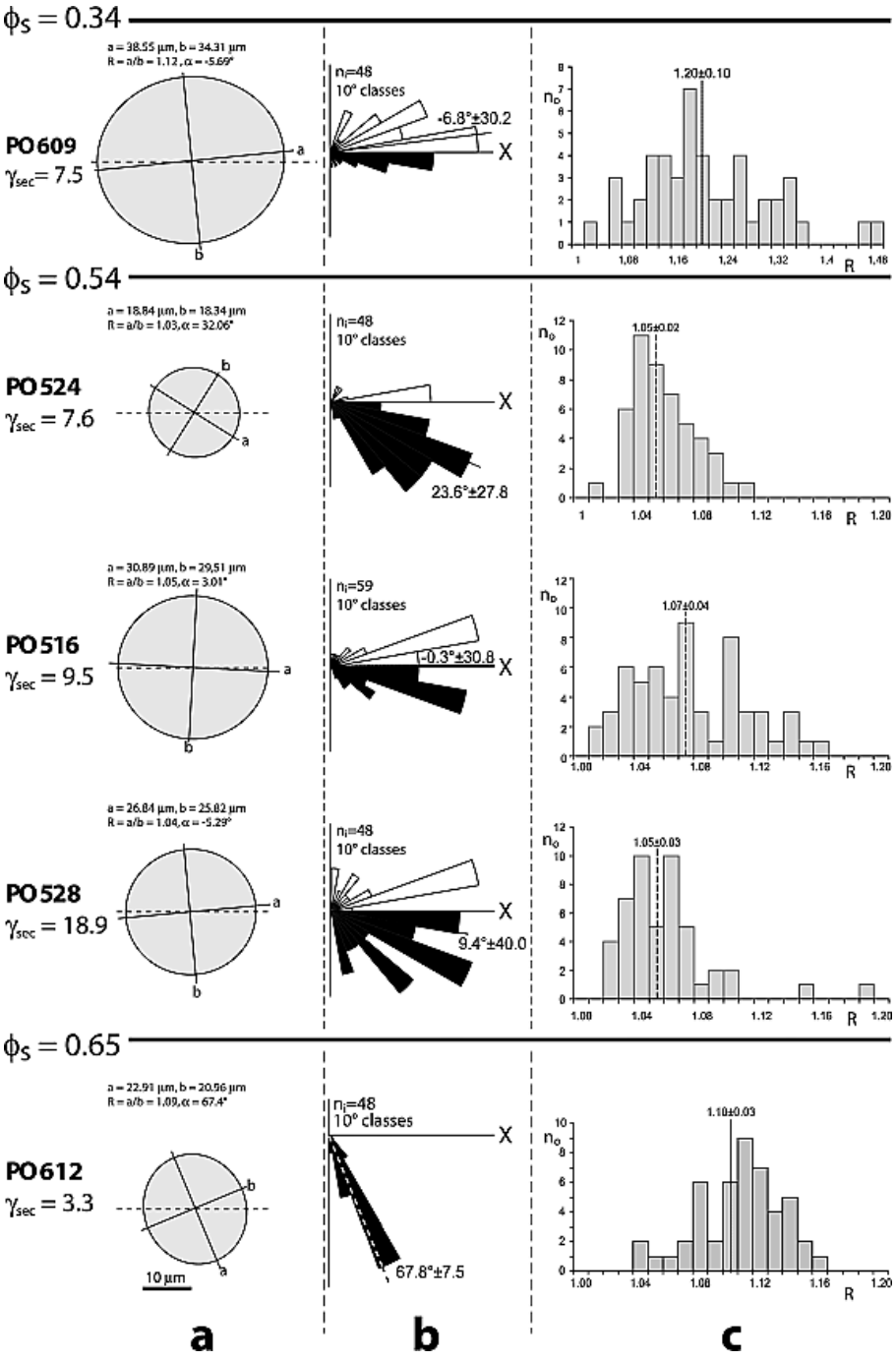

Figure 11. Shape fabrics of alumina grain populations in samples with various solid fractions (φ_s = 0.34, 0.54, and 0.65) deformed to different finite strains. (a) Shape fabric ellipses determined on [XZ] sections using the intercept method and expressed for each ellipse by average long axis a, minor axis b, aspect ratio R = a/b, and orientation α of the long axis. (b) Rose diagram of α and (c) frequency distribution of R determined using the same method of analysis. Dashed lines indicate the arithmetic mean for α and R, and corresponding numerical values are the arithmetic mean and standard deviation. In the rose diagrams, white segments are "positive" orientations, and black segments are "negative" orientations following the sign convention shown in Figure 7. Enhanced EPS

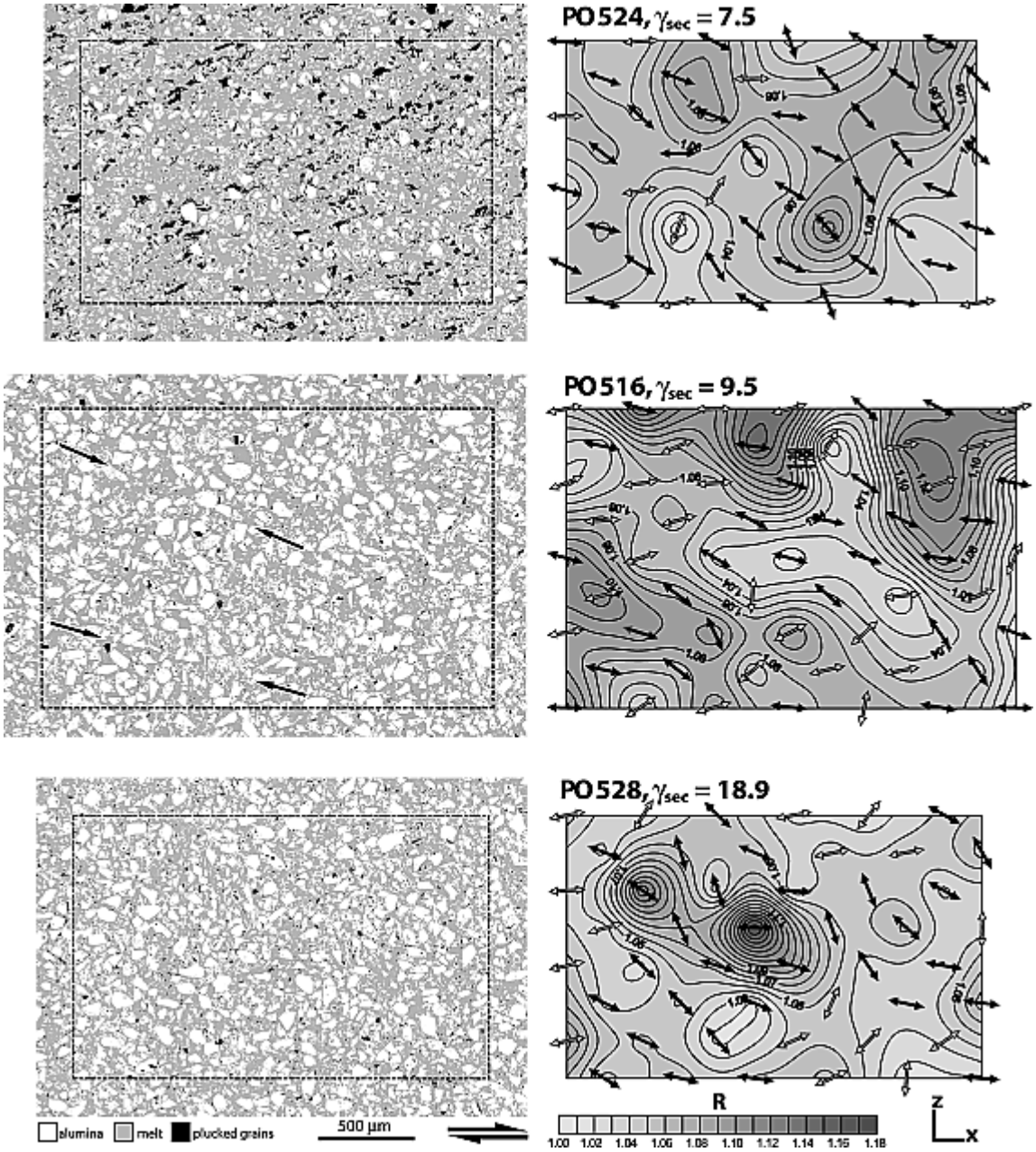

Figure 12. (left) False grey-level images of [XZ] sections of samples with φ_s = 0.54 deformed to different finite strains (sectional strains indicated by γ_{sec}). Dashed black squares delimit areas used for R mapping. Black arrows point out the orientation and delimit the extent of discrete shear bands. (right) R maps. All symbols and calculation procedures are as in Figure 10. Enhanced EPS

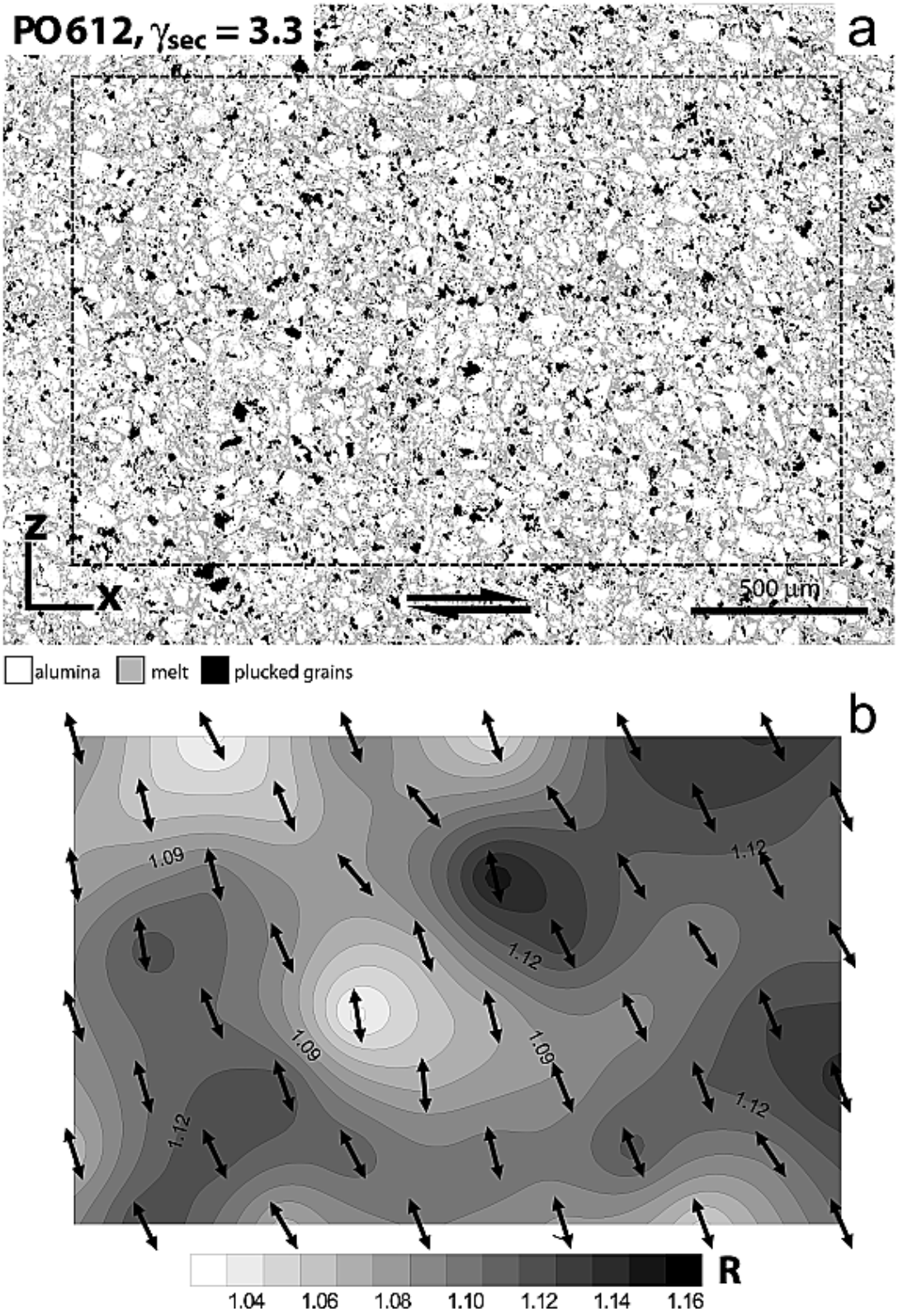

Figure 13. (a) False grey-level images of [XZ] section of deformed sample PO612 (Φ_s = 0.65). Dashed black square delimits the area used for R mapping. (b) R map. All symbols and calculation procedures are as in Figure 10. Enhanced EPS

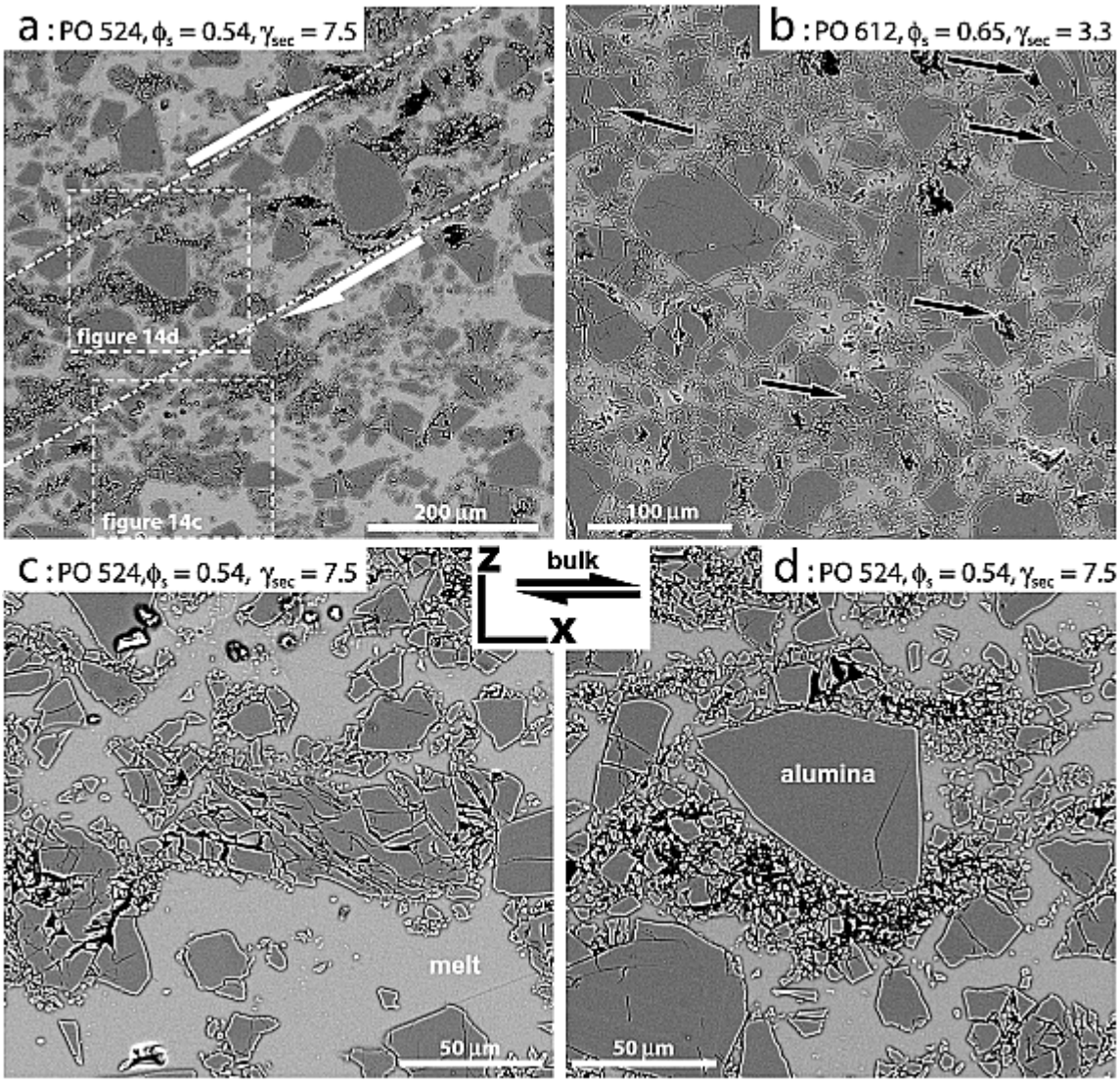

Figure 14. SEM images of structures observed in deformed samples. (a) Shear zone synthetic to the dextral bulk shear strain in PO524 (φ_s = 0.54). Dashed white squares delimit the areas of Figures 14c and 14d. (b) Intense cataclasite texture with widespread fragmentation of grains all over the section in PO612 (φ_s = 0.65). A similar texture can be seen in the whole section in Figure 13. Black arrows point to examples of boudinaged crystals. (c and d) Close views of PO524 (location in Figure 14a). In Figure 14c, outside the shear zone, intragranular fractures developed in a grain whose initial shape is still recognizable, suggesting low finite strain outside the shear zone. In Figure 14d in the shear zone the sense of shear is given by winged porphyroclasts whose asymmetrical wings are composed of dispersed fragments of dislocated grains. Enhanced EPS

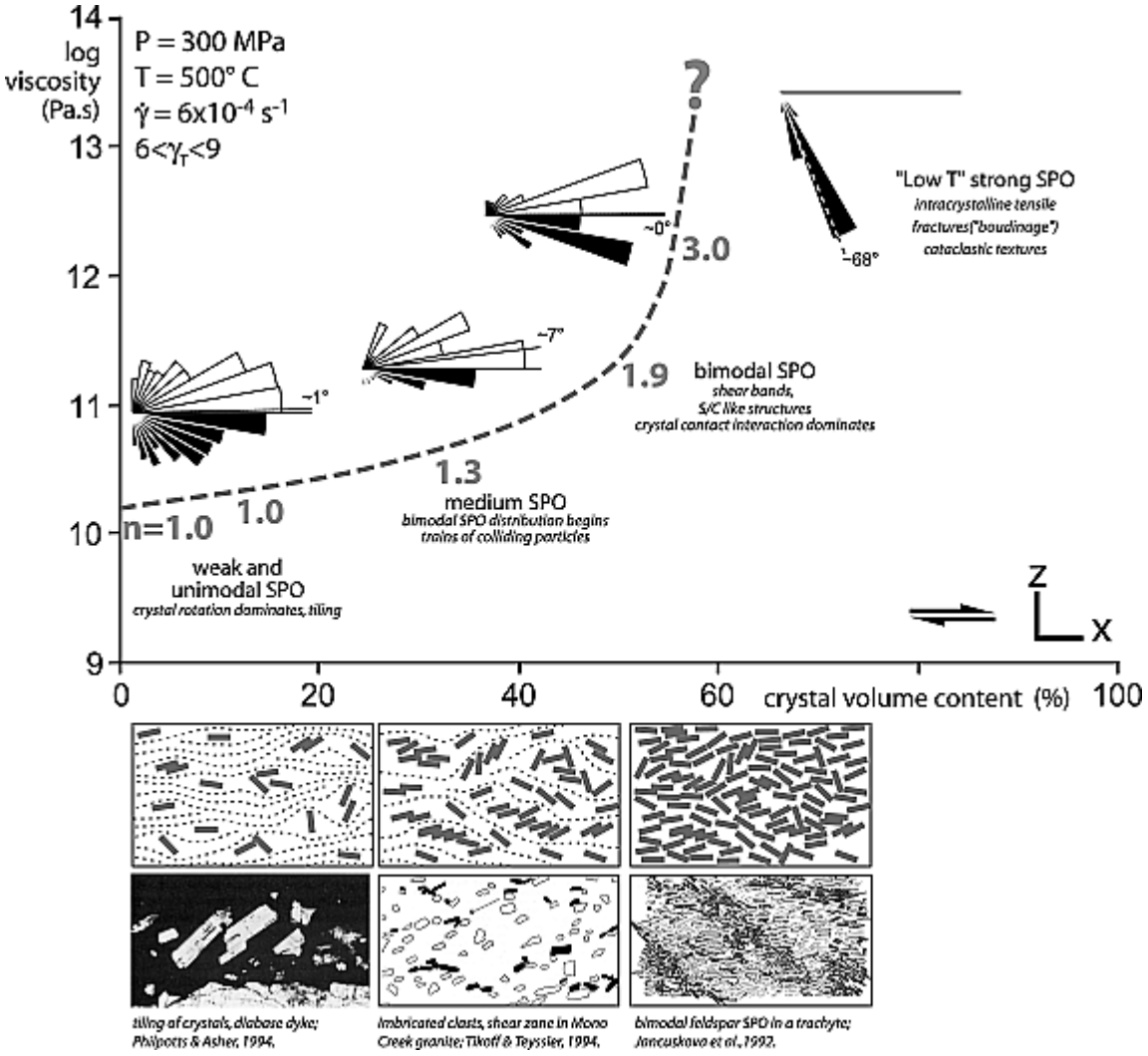

Figure 15. Schematic model for shape fabrics (illustrated by rose diagrams), localization structures, and rheology of an idealized crystallizing magma in the explored $0.0 < \varphi_s < 0.7$ crystallinity range. The dashed curve is the fit found for apparent viscosity at the experimental conditions specified in the diagram (see Figure 5). Grey numbers are the stress exponents determined for the corresponding solid fractions φ_s. Below the graph are schematized 2-D structures illustrated by field examples. Enhanced EPS

Tables

Right-click (PC) or CTRL-click (Mac) to download tab-delimited version: table1.txt

Table 1. Deformation Conditions for Torsion Experiments on Synthetic Magmatic Suspensions

Run	Solid Fraction, vol %	Starting Sample	T, °C	Strain Rate Range, s^{-1}	Finite Strain (γ)
PO540	0	HPG - 10a	475–500	2×10^{-4}–2×10^{-3}	8.8
PO514	16.3	HPG - 5a	475	2×10^{-4}–6×10^{-4}	2.6
PO519	16.3	HPG - 5b	500–550	6×10^{-4}	17.5
PO610	16.3	HPG - 11a	500–550	2×10^{-4}–2×10^{-3}	7.0
PO609	34.2	HPG - 8	500–600	1×10^{-4}–2×10^{-3}	8.5
PO516	53.9	HPG - 6a	500–600	2×10^{-4}–2×10^{-3}	10.8
PO524	53.9	HPG - 6b	500	6×10^{-4}	8.8
PO528	53.9	HPG - 6c	550	6×10^{-4}	21.3
PO612	64.5	HPG - 13	500–600	2×10^{-4}–1×10^{-3}	6.5
PO515	75.7	HPG - 7a	800–1000	2×10^{-5}–2×10^{-4}	0.05

Right-click (PC) or CTRL-click (Mac) to download tab-delimited version: table2.txt

Table 2. Summary of Rheological Data for Synthetic Magmatic Suspensions[a]

	Solid Fraction				
	0%	**16.3%**	**34.2%**	**53.9%**	**64.5%**
log (η_{ap}, Pa s)					
475°C	10.8	10.8			
500°C	10.3	10.4	10.8	11.3	
550°C		9.5[b]	10.1	10.8	11.3
600°C				10.4	11.0
Rheological parameters					
Q_{av} = 231 ± 19 kJ/mol					
n	0.95 ± 0.06	0.99 ± 0.20	1.34 ± 0.10	1.93 ± 0.10	3.02 ± 0.21
A, MPa^{-n} s^{-1}	11.27 ± 0.09	11.23 ± 0.23	10.29 ± 0.12	8.31 ± 0.16	5.23 ± 0.37

[a]Here η_{ap} is the apparent viscosity measured for magmatic suspensions with different solid fractions at the given temperatures and a shear strain rate $\dot{\gamma} \sim 6 \times 10^{-4}$ s^{-1}. For the complete mechanical data set, see Champallier et al. [2007]. Q, n, and A are the activation energy, the stress exponent and the preexponential term, respectively, measured for magmatic suspensions with different solid fractions. Errors are given as one standard deviation.
[b]Data considered to be below the detection range of the apparatus.

Right-click (PC) or CTRL-click (Mac) to download tab-delimited version: table3.txt

Table 3. Image Properties and Measured Surface Fractions of the Phases[a]

Image	Size, pixels	Alumina Grains (Surface), %	Bubbles and Plucked Grains (Surface), %	γ_{sec}
514	2368 × 1774	16.1	0.9	2.2
516	2650 × 1898	46.0	1.0	9.5
519	2655 × 1903	16.0	1.0	15.0
524	2616 × 1868	26.9	7.5	7.6
528	2618 × 1872	46.4	1.1	18.9
540	2608 × 1912	0.0	3.0	7.5
609	2624 × 1855	33.0	6.0	7.5
610	2601 × 1898	13.0	3.0	6.1
612	2607 × 1876	48.0	8.0	3.3
HPG5	2502 × 1782	14.3	1.0	
HPG6	2602 × 1876	46.3	6.1	
HPG7	2600 × 1832	64.9	21.5	
HPG8	2607 × 1887	29.0	5.0	
HPG10	2563 × 1843	0.0	1.0	
HPG11	1986 × 1887	16.0	3.0	
HPG13	2636 × 1880	52.0	6.0	

[a]Scale is approximately 0.99 pixels μm^{-1}.